Endogenously generated Dutch-type Aβ nonfibrillar aggregates dysregulate presynaptic neurotransmission in the absence of detectable inflammation

Emilie L. Castranio[1], Merina Varghese[2], Elentina K. Argyrousi[3], Kuldeep Tripathi[4], Linda Söderberg[5], Erin Bresnahan[6,7,8], David Lerner[6,7], Francesca Garretti[6,7], Hong Zhang[3], Jonathan van de Loo[3], Cheryl D. Stimpson[9,10], Ronan Talty[6,7,11], Charles Glabe[12], Efrat Levy[13], Minghui Wang[14], Marjan Ilkov[14], Bin Zhang[14], Lars Lannfelt[3], Brigitte Guérin[15], William D. Lubell[16], Shai Rahimipour[4], Dara L. Dickstein[6,7,9,10], Sam Gandy[1,7,17,18]†, Ottavio Arancio[3]†, and Michelle E. Ehrlich[1,13,19,*]†

[1]Department of Neurology, Icahn School of Medicine at Mount Sinai, New York, NY, 10029, USA.

[2]George & Anne Ryan Institute for Neuroscience, University of Rhode Island, RI, 02881, USA.

[3]Department of Pathology and Cell Biology, Department of Medicine, and The Taub Institute for Research on Alzheimer's Disease and the Aging Brain, Vagelos College of Physicians and Surgeons, Columbia University, New York, NY, 10032, USA.

[4]Bar-Ilan University, Department of Chemistry, Ramat Gan, 5290002 Israel.

[5]BioArctic, Stockholm, SE-112 51 Sweden

[6]Nash Family Department of Neuroscience, Icahn School of Medicine at Mount Sinai, New York, NY, 10029, USA.

[7]Friedman Brain Institute, Icahn School of Medicine at Mount Sinai, New York, NY, 10029, USA.

[8]Department of Hematology and Oncology, Icahn School of Medicine at Mount Sinai, New York, NY, 10029, USA.

[9]Department of Pathology, Uniformed Services University of Health Sciences, Bethesda, MD, 20814, USA.

[10]Henry M. Jackson Foundation for the Advancement of Military Medicine Inc, Bethesda, MD, 20817, USA.

[11]Department of Medicine, Memorial Sloan Kettering Cancer Center, New York, NY, 10065, USA

[12]Department of Molecular Biology and Biochemistry, University of California, Irvine, CA, 92697, USA.

[13]Center for Dementia Research, The Nathan S. Kline Institute for Psychiatric Research, 140 Old Orangeburg Road, Orangeburg, NY, 10962, USA, and New York University Grossman School of Medicine, NYU Langone Medical Center, New York, NY, 10016, USA.

[14]Department of Genetics and Genomic Sciences, Icahn School of Medicine at Mount Sinai, New York, NY, 10029, USA.

[15]Department of Radiochemistry, University of Sherbrooke, Sherbrooke, Quebec, J1K 2R1, Canada

[16]Department of Chemistry, University of Montreal, Montreal, Quebec, H3C 3J7, Canada

[17]Department of Psychiatry and Alzheimer's Disease Research Center, Icahn School of Medicine at Mount Sinai, New York, NY, 10029, USA.

[18]James J Peters VA Medical Center, Bronx, NY, 10468, USA.

[19]Department of Pediatrics, Icahn School of Medicine at Mount Sinai, New York, NY, 10029, USA.

† Contributed equally to supervision

* Correspondence: michelle.ehrlich@mssm.edu

Abstract (166 words)

APP^{E693Q} transgenic mice develop aging-related learning deficits and accumulate endogenously generated nonfibrillar aggregates of Aβ (NFA-Aβ) and APP α-carboxy terminal fragments. The *APP*^{E693Q} mutation disrupts amyloid fibril formation, and no plaques develop in these mice. In the current study, the aging-related accumulation of NFA-Aβ in *APP*^{E693Q} mice was revealed by A11 immunohistochemistry and NFA-Ab-detecting cyclic D,L-α-peptide-FITC microscopy. The presynaptic termini of *APP*^{E693Q} mice developed aging-related physiological abnormalities in post-tetanic potentiation, synaptic fatigue, and synaptic vesicle replenishment. Single-cell RNA sequencing showed that excitatory neurons exhibited the most altered transcriptomic profile, especially involving "protein translation" and "oxidative phosphorylation". Direct measurements of electron transport chain catalysis revealed reduction in mitochondrial complex I activity in Dutch mice. Microglial transcript analysis revealed no evidence of inflammation. The incomplete clinical response to fibrillar Aβ immunodepletion in human patients may be attributable to residual NFA-Aβ that are undetectable by currently available biofluid or neuroimaging biomarkers. The depletion or neutralization of both fibrillar and NFA-Aβ may be needed for complete elimination of Aβ toxicity.

Teaser

APP^{E693Q} "NFA-Aβ only" mice reveal clinically relevant mechanisms despite the absence of detectable inflammation

Introduction

Synaptic dysfunction is believed to be a key pathological hallmark of Alzheimer's disease (AD) that begins gradually and parallels clinical cognitive decline (*1-4*). Many studies have demonstrated that the burden of fibrillar amyloid-β (Aβ) proteinopathy does not correlate with synaptic loss (*5-7*) or with cognitive status(*8*). Instead, some investigators have proposed that brain levels of synaptotoxic nonfibrillar aggregates of Aβ (NFA-Aβ) including Ab oligomers and protofibrils correlate more closely with synaptic loss (*9, 10*). Synaptic NFA-Aβ has been detected in AD brains, and NFA-Aβ levels in human brain synaptosomes can differentiate subjects with early AD from cognitively intact controls with AD pathology (*11-13*). *In vitro*, synthetic NFA-Aβ peptides can cause inhibition of long-term potentiation (LTP) in hippocampal slices (*14, 15*), while *in vivo* injections of NFA-Aβ into the cerebral ventricles of healthy rats leads to cognitive deficits (*16*). Studies using a transgenic mouse model of AD have demonstrated that neuronal loss in the hippocampus correlates with NFA-Aβ levels but not with amyloid plaque burden (*17*). In 2010, we reported a transgenic mouse model overexpressing Dutch mutant human amyloid precursor protein (*APP*^{E693Q}) on the pan-neuronal Thy1 promoter (*18*). This mutation within the Aβ domain substitutes a glutamine for glutamic acid, thereby disrupting fibril assembly and favoring the formation of NFA-Aβ. The *APP*^{E693Q} mutation causes hereditary cerebral hemorrhage with amyloidosis - Dutch type (HCHWAD) (*19*). The neuropathology of HCHWAD shows prominent cerebrovascular amyloidosis and hemorrhage as well

69 as diffuse parenchymal Aβ deposition (*20*). Although the *APP*^{E693Q} (or "Dutch") transgenic mouse failed to
70 recapitulate the full neuropathology of either AD or HCHWAD, we were struck by the aging-related development
71 of learning behavior impairment that was observed in the absence of detectable fibrillar Aβ. Analysis of the Dutch
72 mouse brain revealed that this learning behavior impairment was directly related to the brain levels of NFA-Aβ
73 (*18, 21*), an observation supported by imaging data in the current paper using epitomic histochemistry with anti-
74 prefibrillar oligomer-specific antibody A11 (*97*) and NFA-Aβ-detecting cyclic peptide-FITC fluorescence
75 microscopy (*22*). The Dutch mice also exhibit detectable cerebrovascular Aβ deposition and traces of perivascular
76 iron (presumably due to the extravasation of red blood cells) without overt hemorrhage. The reported
77 accumulation of APP α- and β-carboxyl-terminal fragments (APP-CTFs) in the Dutch mouse brain has raised the
78 possibility that the learning impairment might be at least partially attributable to APP-CTF proteinopathy alone
79 or in combination with the NFA-Aβ proteinopathy (*23*).

80 A detailed study of hippocampal CA1 neurons reported that significant decreases in dendritic length and
81 complexities of apical, but not basal, dendrites were observed in Dutch compared to wildtype mice (*24*). The
82 synaptic ultrastructure in the same brain region revealed no differences in overall synaptic density or morphology.
83 A significant reduction in the postsynaptic density (PSD) length of synapses was identified on mushroom spines
84 in Dutch mice compared to those of wildtype littermates. In the current study, electrophysiological and immuno-
85 electron microscopy approaches were employed to investigate the excitatory synapses in the hippocampus of the
86 Dutch mouse.

87 Bulk sequencing of RNA from the entorhinal cortex and dentate gyrus of Dutch mice revealed entorhinal
88 cortex profiles that correlated with several human late-onset AD signatures (*25*). Microglial signatures were
89 enriched in the differentially expressed genes (DEGs). Differential exon usage was also prominent in the Dutch
90 mouse entorhinal cortex and the PSAPP (*APP*$^{KM670/671NL}$/*PSEN1*$^{\Delta exon9}$) mouse dentate gyrus. The transcriptomes
91 from the entorhinal cortex and the dentate gyrus of Dutch mice were also enriched in markers of glutamatergic
92 neurons, synaptic transmission, and protein translation. To study transcriptomics in the Dutch mouse
93 hippocampus, single-cell RNA sequencing (scRNA-seq) was employed and revealed dysregulation of pathways
94 for protein translation, oxidative phosphorylation, and the electron transport chain. Direct measurements of
95 electron transport chain catalysis revealed changes in activity of mitochondrial complex I but not in that of
96 complexes II, III, or IV.

97 In summary, a multi-disciplinary analysis of the Dutch mouse has now revealed alterations in synaptic
98 physiology, gene expression, and protein translation in excitatory neurons, as well as changes in the transcriptomic
99 profile and mitochondrial morphology and activity. Moreover, the high sensitivity of scRNA-seq has enabled
100 neuroinflammation to be ruled out as a major contributor to pathogenesis in the hippocampi of Dutch mice. The
101 present studies are among few focusing on endogenous generation of NFA-Aβ without the concurrent presence

102 of potential confounds from either Aβ fibrils or synthetic peptides. These findings support the notion that fibrillar
103 Aβ is not necessary for the aging-related learning deficit observed in Dutch mice. These data may have important
104 implications for the genesis of cognitive impairment in humans. The clinical response to anti-amyloid antibody
105 therapy may be dampened due to the persistence of toxic NFA-Aβ conformers that go undetected in contemporary
106 analysis of fluid biomarkers and in amyloid fibril positron emission tomography (PET) imaging. Depletion or
107 neutralization of NFA-Aβ may be required for complete elimination of clinically relevant Aβ toxicity.
108

109 **Results**

110 ***Dutch mice show increased levels of nonfibrillar aggregate with aging.***

111 Aging-dependent investigation of the Dutch mice revealed that 12 months is the first age at which deficits
112 attributable to NFA-Aβ can be detected (*18*). To determine the involvement of NFA-Aβ in brain changes, multiple
113 analyses were conducted at different ages, before and after the appearance of NFA-Aβ. Epitomic characterization
114 was performed on cortical tissue from 2- and 24-month-old Dutch mice. Interestingly, this characterization
115 revealed a significant increase with aging in the A11/6E10 ratio (ratio of prefibrillar oligomer content to total Aβ
116 content; $F(3,16) = 17.05$; $p<0.0001$), but no such aging-related change in the OC/6E10 ratio (ratio of fibrillar oligomer
117 content to total Aβ content; $F(3,16) = 2.557$; $p=0.0916$) in Dutch mice (**Figure 1, Supplementary Figure 1A**).
118 Furthermore, brains were analyzed for the presence of protofibrils (PF) using the homogenization protocol
119 described in Tucker *et al.* (*26*) and assayed for PF levels in the TBS soluble fraction using a mAb158-mAb158
120 sandwich MSD assay employing an in-house synthetic protofibril as calibrator. Both assays showed very low
121 levels of Aβ PF. In the mAb158 sandwich assay, Aβ PF levels were around 100 pM, levels indistinguishable from
122 those in homogenates of wildtype mice (**Supplementary Figure 1B**). No PF were detected in the cerebellum.
123 Levels of PF in Dutch mice were approximately 10- to 100-fold lower than those measured in Tg-APP^{ArcSwe} and
124 Tg2576 (depending on age analyzed). In addition, $A\beta_{38/40/42}$ fragments were analyzed in the TBS insoluble pellet
125 fraction after dissolution in formic acid and neutralization. Levels of Aβ PF were again very low, consistent with
126 the absence of parenchymal plaques in Dutch mice.

127 The elevation of NFA-Aβ levels in the cortex, thalamus, and hippocampus of Dutch mice was visually and
128 morphologically confirmed using a combination of immunohistochemistry using A11 antibody and fluorescence
129 microscopy employing cyclic D,L-α-peptide-2 (CP-2)-FITC as a fluorescein-tagged NFA-Aβ-detecting ligand
130 (*22*) (**Figure 1, Supplementary Figures 1C and 2-3**). The hypothesis that CP-2 and A11 bind to similar or
131 identical domains on NFA-Aβ was confirmed by cross-competition blocking experiments in which pre-incubation
132 of brain slices with CP-2 peptide prevented the subsequent binding of the prefibrillar oligomer-specific antibody
133 A11 (**Supplementary Figure 4**). Furthermore, the interaction of CP-2 with NFA-Aβ has been characterized (*99-*

134 *103*): CP-2 was demonstrated (1) to stabilize Aβ dimers and trimers using a photoinduced cross-linking of
135 unmodified proteins (PICUP) assay (*99-102*) and (2) to bind 10 nm particles typical of NFA-Aβ (*103*). In the
136 current study, CP-2 exhibited similar K_d values for both fibrillar and nonfibrillar forms of Aβ in surface plasmon
137 resonance (SPR) assays (**Supplementary Methods**): CP-2 interacted with Aβ fibrils and NFA-Aβ with K_d values
138 of 6 and 4 μM, respectively.
139
140 ***Dutch mice showed no significant impairment in basal synaptic transmission and long-term synaptic***
141 ***plasticity in the hippocampus.***
142 The relationship between synaptic input strength and the resulting electrical response, the so-called "input-
143 output relation" and long-term potentiation (LTP) were tested in 7- to 7.5-month-old and 10.5- to 11-month-old
144 Dutch mice. The two genotypes displayed similar input-output relationships and LTP in both age groups,
145 suggesting that basal synaptic transmission at the CA1 region of the hippocampus and long-term synaptic
146 plasticity at the Schaffer collateral were unimpaired in Dutch mice **(Figure 2**).
147
148 ***Dutch mice showed no change of hippocampal mGluR-2/3 expression or of mGluR-2/3+ synapse density.***
149 Comparable levels of mGluR-2/3 protein were observed in Western blots of the insoluble membrane fraction
150 from the hippocampus of 12-month-old wildtype and Dutch mice (**Supplementary Figure 5A**). Since Western
151 blots may not detect regional differences, array tomography and immunofluorescence were used to analyze
152 mGluR-2/3 puncta after staining serial sections of CA1 neurons with Neurotrace (**Supplementary Figure 5B**).
153 Comparable densities in the CA1 of wildtype and Dutch mice were observed in 3D reconstructions of mGluR-
154 2/3 synaptic puncta by array tomography (**Supplementary Figure 5C**, $F_{(4,3)} = 1.476$, $p = 0.7802$). Quantification
155 of the total mGluR-2/3 puncta output yielded an average tissue density (puncta/μm^3) of 0.275 ± 0.087 for wildtype
156 mice and 0.322 ± 0.112 for Dutch mice. Both genotypes exhibited comparable puncta size ranges, and no
157 significant difference in average mGluR-2/3 puncta size (**Supplementary Figure 5D**; $F_{(1,3)} = 0.751$, $p = 0.538$)
158 per percentile per sample. Similarly, neither the density nor size of GluN1 puncta were altered in Dutch mice
159 (**Supplementary Figure 5E-F**; $F_{(4,3)} = 1.431$, $p = 0.8003$ for density and $F_{(1,3)} = 0.116$, $p = 0.950$ for puncta size).
160
161 ***Dutch mice had larger PSD area on small mGluR-2/3$^+$ synapses in the CA1 region.***
162 Changes in mGluR-2/3$^+$ excitatory neurons were examined at the ultrastructural level in 12-month-old mice.
163 Comparable percentages of mGluR-2/3$^+$ synapses among total, non-perforated, and perforated synapses in the
164 CA1 were observed in Dutch and wildtype mice using immunogold EM against mGluR-2/3 (**Figure 3A-C**).
165 Moreover, Dutch and wildtype mice exhibited no difference in the total and perforated synapses (**Figure 3D, F**).

166 Higher postsynaptic density (PSD) area of non-perforated mGluR-2/3^{+} synapses was detected in the Dutch
167 compared to wildtype mice (**Figure 3E**), both of which had comparable distributions of mGluR-2/3^{+} particles per
168 PSD area (**Figure 3G-I**).
169
170 ***Dutch mice exhibited defects in PTP, SF, and replenishment of the vesicle pool after depletion.***
171 We assessed several mechanisms related to function of the presynaptic terminal. 11- to 13-month-old Dutch
172 mice and their wildtype littermates showed the same response in paired-pulse facilitation (PPF) **(Figure 4A)**, a
173 type of short-term plasticity that is most likely dependent upon the build-up of Ca^{2+} in the presynaptic neuron due
174 to the close pairing of two action potentials. Accumulation of Ca^{2+} in the presynaptic neuron results in increased
175 neurotransmitter release and subsequently increased response after the arrival of the second action potential(*27*).
176 Accordingly, facilitation is no longer present when a long-time interval (1 second) is introduced between the two
177 stimuli. Both wildtype and Dutch mice showed increased facilitation at short time intervals, and no difference was
178 observed between the two genotypes. In contrast to PPF, Dutch mice showed decreased post-tetanic potentiation
179 (PTP) when compared to wildtype mice **(Figure 4B)**. PTP is performed in the presence of D-2-amino-5-
180 phosphonovalerate (D-APV) that blocks NMDA receptors, thereby preventing the onset of plasticity through
181 NMDA-dependent postsynaptic mechanisms that might interfere with its measurement. Due to the DAPV, the
182 fEPSP slope declines back to baseline a few seconds after stimulation. PTP is another form of short-term plasticity
183 and reflects the enhanced release of neurotransmitter due to the increased levels of Ca^{2+} at the presynaptic terminal
184 during the tetanic stimulation(*28*).
185 We also studied the effect of the Dutch mutation on the efficacy of presynaptic mechanisms by examining
186 synaptic fatigue (SF) and replenishment of the vesicle pool after its depletion. Both mechanisms appeared to differ
187 between wildtype and Dutch mice. Specifically, the rate of decay examined with SF was faster for the Dutch mice
188 as compared to wildtype **(Figure 4C),** whereas the growth rate during the replenishment phase was higher in the
189 Dutch in comparison to wildtype **(Figure 4D).** The decline in the slope that is observed during SF is thought to
190 represent the depletion of the readily releasable pool (RRP) of neurotransmitter that resides in vesicles at the
191 presynaptic cells, while replenishment depicts the refilling process of the RRP after its depletion with high
192 frequency stimulation. Mechanistically, it has been suggested that both SF and replenishment are dependent on
193 accumulation of residual Ca^{2+} at the presynaptic terminal(*27, 28*).
194
195 ***Dutch mice exhibited no change in vesicle size or number of docked vesicles but show a trend towards fewer***
196 ***vesicles in the reserve pool at presynaptic terminals in the CA1.***
197 The size, number, and distribution of vesicles were quantified within the presynaptic terminal of 12-month-
198 old mice. No differences were observed in synaptic vesicle sizes at the presynaptic terminal nor the number of

199 docked vesicles at the synapses of the active zone in Dutch and wildtype mice (**Supplemental Figure 6A-C, E,**
200 **G**). A decline in the number of synaptic vesicles was found in the reserve pool beyond 300 nm from the active
201 zone of Dutch compared to wildtype mice, but did not reach statistical significance and appeared to be driven by
202 vesicles in large synapses (**Supplemental Figures 6D and 6H**). The hippocampi of Dutch and wildtype mice
203 exhibited no differences in the levels of either the postsynaptic density protein of 95kDa (PSD95) or the
204 presynaptic marker synaptophysin (**Supplemental Figure 7**).
205
206 ***Dutch mice had no change in synaptic distribution of mGluR-2/3+ in the CA1.***
207 Comparable distributions of mGluR-2/3 were observed by immunogold labeling and electron microscopy
208 (EM) at the synapse (**Figures 5A-C**), pre- and postsynaptic compartments (**Figure 5D**), presynaptic active zone,
209 synaptic cleft, peri-synaptic area, postsynaptic membrane, and postsynaptic cytoplasm (**Figure 5E**) in 12-month-
210 old wildtype and Dutch mice.
211
212 ***Dutch mice display shared gene expression profiles across multiple cell types.***
213 Employing brains from Dutch mice alongside sex- and age-matched wildtype littermates, scRNA-seq was
214 performed. Hippocampi were collected from mice at 12 months, an age characterized by established cognitive
215 deficits and high levels of NFA-Aβ and α-CTF in Dutch mice(*18*). After quality control filtering (**Supplementary**
216 **Figure 8**), 61,642 (32,661 Dutch and 28,981 wildtype) cells were isolated from thirteen distinct clusters which
217 were identified based on the expression of well-known cell-type-specific markers **(Figure 6A-B**, **Supplementary**
218 **Tables 1-2).** Pseudo-bulk differential expression analysis was used to identify gene expression changes within
219 each cell type. For further analysis (C0-6), clusters of interest were identified based on differentially expressed
220 genes (DEGs; adj. p-value cutoff <0.05) (**Figure 6C-D**, **Supplementary Figures 9-12, Supplementary Table**
221 **3**).
222 Faced with considerable overlap in DEGs, the clusterProfiler(*29*) approach was employed to compare
223 biological themes and identify the Gene Ontology (GO) term enrichment shared among the gene clusters. Among
224 the shared terms were "structural constituent of ribosome" (example genes include: *Rpl23, Rpl30, Rpl37a, Rpl6,*
225 *Rpl9, Rps24*) **(Figure 7A-B)**, and "amyloid-beta binding" (*Apoe, Atp1a3, Clu, Cst3)* **(Figure 7A, C)**. The shared
226 DEGs and GO terms across clusters were similar to a previously identified "aging signature" in mouse brain(*30*),
227 in which ribosomal protein genes, long noncoding RNA genes (e.g., *Malat1*) as well as ribosome-related pathways
228 and processes, all were significantly affected in 21- to 22-month-old mouse brain across multiple cell types
229 compared to that of their 2-to 3-month-old counterparts. Across clusters, 453 DEGs were found to overlap with
230 the aging-related gene list **(Figure 7D)**, from which 435 genes displayed the same directionality across all clusters
231 (389 upregulated and 46 downregulated, **Figure 7E**) as reported.(*30*).

232

233 ***Dutch mice do not show obvious differences in microglial gene expression.***

234 In many Aβ-depositing mouse models of AD, microglia show prominent transcriptional responses and
235 increased microgliosis with conspicuous peri-plaque localization(*31, 32*). Additionally, the microglial immune
236 response to NFA-Aβ has been implicated as an early, key step in AD pathogenesis. To investigate the microglial
237 responses in more detail, we performed subclustering analysis, which revealed three subpopulations of microglia
238 in the hippocampus (**Figure 8A**). None of the subpopulations showed higher abundance in either genotype. The
239 subpopulations also did not segregate based on expression of established microglial profile markers, such as
240 homeostatic, disease-associated microglia (DAM)(*33*), type I interferon-induced (IFN), or major
241 histocompatibility complex-expressing (MHC) signatures(*34*) (**Figure 8B**). Expression of homeostatic markers
242 was high in all microglia subpopulations and did not change in microglia from the hippocampus of Dutch mice
243 (**Figure 8C**). Additionally, no differences were seen in IBA1 IHC between 12-month-old Dutch and wildtype
244 mice **(Supplementary Figure 13A-B)**. Notably, we also did not find an increase in colocalization of C1q and
245 PSD95 puncta in 12-month-old Dutch mice **(Supplementary Figure 13C)**, as was reported in J20 mice(*35*).

246

247 ***Dutch mice show changes in gene expression associated with translation in excitatory neurons.***

248 Cluster 6 was identified as excitatory neurons and showed the most extensive and unique transcriptional
249 response in Dutch mice (**Figure 6C-D, Figure 9A**). In the GO term analysis, upregulated Cluster 6 DEGs included
250 "cytoplasmic translation" (*Eif2s2, Eef1a1, Eef1b2, Rpl22, Rpl26, Rpl27*) and "negative regulation of amyloid
251 fibril formation" (*Cryab, Pfdn6, Slc25a4, Grin2b, Stmn1, Smad4, Pik3r1*) **(Figure 9B, Supplementary Table 4).**
252 Notably, "regulation of synapse organization" was also among the top GO terms (*Cask, Cdh8, Gpc4, Grin2b,*
253 *Mef2c, Nrxn1, Pafah1b1, Ptprd, Tuba1a, Ube2v2, Malat1, Opa1, Mycbp2, Nrcam, Il1rapl1, Arhgef9*), a selection
254 of which are also highlighted in **Figure 9A**. In the GO term analysis, downregulated Cluster 6 DEGs included
255 those related to processes associated with mitochondrial bioenergetic function, i.e., "electron transport chain"
256 (*Mt-Co1, Mt-Co3, Mt-Cytb, Ppp1cb, Calm2*) and "oxidative phosphorylation" (*mt-Atp6, mt-Nd1, mt-Nd3)*
257 (**Figure 9C, Supplementary Table 5**). A selection of unique DEGs from Cluster 6 is shown in **Figure 9D.**

258 Gene expression was also examined for biological processes associated with presynaptic mechanisms and
259 synaptic transmission, specifically "regulation of synapse organization", a subset of "regulation of cell
260 morphogenesis" (**Supplementary Figure 14A**). Myocyte Enhancer Factor 2C (*Mef2c*) is among this gene list
261 and has been identified as a candidate risk gene for developing late onset Alzheimer's disease (LOAD)(*36, 37*).
262 Considering that oligodendrocytes can modulate presynaptic properties and synaptic transmission(*38, 39*),
263 relevant biological processes such as "modulation of chemical synaptic transmission" were assessed and found
264 among the top biological processes in Cluster 4 oligodendrocytes (**Supplementary Figure 14B, Supplementary**

265 **Table 6)**. Approximately 25% of the genes present in this biological process are among DEGs in Cluster 6. Genes
266 associated with synaptic transmission that were among those specific to Cluster 4 included transferrin (*Trf),* a
267 recently identified biomarker of AD(*40*), and carbonic anhydrase 2 (*Car2*). Carbonic anhydrase inhibitors have
268 been considered for prevention of neurovascular dysfunction in CAA and AD due in part to their ability to prevent
269 mitochondrial dysfunction and oxidative stress (*41, 42*).

270 A cell-cell communication analysis was performed using the software tool Cellphone DB to compute
271 interactions between clusters based on the known Ligand-Receptor (LR) pairs (**Supplementary Table 7**). For
272 each LR in each sample, the software estimated the interaction strength from Cluster 4 oligodendrocytes to Cluster
273 6 excitatory neurons, from which differences in interaction strengths between Dutch and WT mice were evaluated
274 by t-test. Twelve LR pairs showed significant interaction difference at p-value ≤ 0.05, and all twelve presented
275 higher interactions in Dutch mice. Among these LRs, *Gabbr2* was up-regulated in the Cluster 6 excitatory neurons
276 in Dutch mice compared to those of wildtype (log2FC = 0.19, adj. p-value = 3.6E-4). In Dutch compared to
277 wildtype mice, stronger interactions were exhibited by *Gabbr2* with multiple GABA inhibitory neurotransmitter
278 complex partners including GAD2, SLC6A11, SLC6A1, SLC6A8, SLC6A6, and SLC32A1.

279

280 ***Dutch mice have fewer and smaller mitochondria in CA1 presynaptic boutons.***

281 The number and morphology of mitochondria were assessed in the presynaptic terminals of excitatory neurons
282 in the *stratum radiatum* of wildtype and Dutch mice (**Figure 10A, B**). Previously, NFA-Aβ has been reported to
283 cause imbalance in mitochondrial fission-fusion, leading to fragmented morphology and altered function(*43-47*).
284 Fewer presynaptic mitochondria were found in Dutch compared to wildtype mice (**Figure 10C**, mean ± SD for
285 total of mitochondria per presynaptic bouton = 106.3 ± 20.06 in wildtype and 75.60 ± 14.62 in Dutch, p= 0.0324
286 by two-tailed unpaired t test). This deficiency in the Dutch mice was likely due to fewer straight mitochondria at
287 the presynaptic terminals, because curved mitochondria numbers were unchanged between genotypes (**Figure**
288 **10D-F**, mean ± SD for number of straight mitochondria = 101.3 ± 17.95 in wildtype and 71.80 ± 15.06 in Dutch,
289 p= 0.314 by two-tailed unpaired t test. Mean ± SD for number of curved mitochondria = 5.00 ± 2.16 in wildtype
290 and 3.80 ± 2.59 in Dutch). In assessments of differences in morphology, mitochondrial diameters were
291 comparable (**Figure 10G**, mean ± SD = 328.6 ± 19.29 in wildtype and 301.8 ± 28.73 in Dutch), but shorter lengths
292 were found in 12-month-old Dutch compared to wildtype mice, as estimated from the number of layers traversed
293 in the consecutive sections by each mitochondrion (**Figure 10H**). Each layer traversed was ~ 80 nm using 3-
294 dimensional reconstruction of measurements from serial sections.

295

296 ***Dutch mice have reduced mitochondrial electron transport chain complex I activity.***

297 The activities of electron transport chain complexes I-IV and citrate synthase were assessed in hippocampi
298 from 7- and 12-month-old wildtype and Dutch mice as described(*104, 105*). Each complex activity was
299 standardized to either μg protein (p=0.0355) or to mU/ml of citrate synthase (CS) and analyzed using an unpaired
300 t test (p=0.0197) (**Supplemental Figure S15, Supplemental Tables 8, 9**). Compared to that of wildtype,
301 mitochondrial complex I activity was reduced in 12- but not 7-month-old Dutch mice.
302

303 **Discussion**

304 The purpose of this study was to elucidate the molecular pathogenesis underlying the learning behavioral
305 deficits exhibited by the Dutch mouse model which accumulates NFA-Aβ and APP α-CTFs but never forms
306 amyloid fibrils. Our study adds to the few that have detected endogenously generated NFA-Aβ without concurrent
307 presence of fibrils or the presence of synthetic peptides. The location of Dutch NFA-Aβ in the mouse brain was
308 ascertained using immunohistochemistry with A11 antibody and fluorescence microscopy with a cyclic peptide-
309 FITC ligand(*22*). In contrast to the apparently normal density and morphology of synapses in excitatory neurons,
310 we observed abnormalities in the apical dendrite structure in the CA1 of Dutch mice(*24*). Therefore, we sought
311 to determine whether Dutch mice exhibit plasticity impairment during growth from 7 to 13 months, before and
312 after NFA-Aβ aggregation can be detected in the brain. A variety of electrophysiological techniques were used to
313 examine short- and long-term synaptic plasticity. Although no changes in basal synaptic transmission nor long-
314 term synaptic plasticity were observed at the CA1-CA3 area of the hippocampus in slices obtained from young
315 (7- to 7.5-month-old) and old (10.5- to 11-month-old) Dutch mice, impaired short-term synaptic plasticity
316 developed at the CA1-CA3 synapses first appearing at the age of 11 to 13 months.
317 Assessment of the I-O curve and the LTP response after high frequency stimulation in the CA1-CA3 synapses,
318 indicated no difference between Dutch and wildtype genotypes, suggesting that NFA-Aβ and/or APP α-CTFs
319 affect neither spontaneous activity nor the long-term plasticity in the examined age window. In contrast,
320 intracerebroventricular injection of synthetic Dutch and Arctic (APP^{E693G}) Aβ peptides have been previously
321 reported to block LTP in rats(*48*). Long-term plasticity changes may possibly be manifested only in older Dutch
322 mice. In addition, changes may occur in other types of long-term synaptic plasticity such as long-term depression,
323 as well as in other areas of the hippocampus, such as mossy fiber-CA3 synapses. Despite normal *long-term*
324 synaptic plasticity in young or old Dutch mice, defects in several types of *short-term* plasticity emerged in the
325 aging 11- to 13-month-old Dutch mice. Specifically, mice carrying the Dutch mutation exhibited impaired PTP,
326 synaptic fatigue (SF), and impaired replenishment of the synaptic pool, but unaffected PPF. Both PPF and PTP
327 are related to accumulation of Ca^{2+} at the presynaptic terminal, due (respectively) to two closely paired pulses or
328 to high frequency stimulation, both of which augment neurotransmitter release. Although impaired PTP without

329 changes in PPF might seem contradictory, previous studies have shown that PPF and PTP are governed by
330 different synaptic vesicle proteins. Specifically, the absence of the synaptic vesicle protein synaptogyrin I in mice
331 causes impaired PTP, but its absence has no effect on PPF(*49*). More in-depth investigation of synaptic vesicle
332 proteins is required to elucidate the molecular mechanisms underlying impaired plasticity in Dutch mice.

333 Our earlier studies identified abnormalities in the dendritic structure of excitatory neurons in the CA1 of Dutch
334 mice(*24*). Although mGluR2 is necessary for synaptic binding of oAβ, and mGluR3 has been reported to mediate
335 the effects of NFA-Aβ on synaptic function (*50, 51*), the CA1 of Dutch and wildtype mice exhibited similar
336 synaptic density of mGluR-2/3^{+}. Moreover, similar levels of mGluR-2/3 were observed in the hippocampus as
337 well as the pre- and postsynaptic compartments of axospinous synapses in the CA1 of Dutch and wildtype mice.
338 In contrast, mGluR-2/3 expression was previously reported to be reduced in the CA1 of AD patients(*52, 53*),
339 depending on which hippocampal subfield was examined(*53, 54*). Furthermore, in primary rat neurons treated
340 with NFA-Aβ, mGluR-2/3 levels initially increased as the immediate response but decreased following activation,
341 suggesting that synaptic activity contributes to the effect of NFA-Aβ on receptor subunit expression (*55*). In CA1
342 synapses in the Dutch mice, differences were identified in the greater PSD area of small mGluR-2/3^{+} synapses
343 and in the reduced number and size of presynaptic mitochondria (discussed below in the context of the
344 transcriptomic data). Recruitment of mGluR1 or NMDA receptors to the PSD in the presence of NFA-Aβ could
345 be a possible explanation for our finding of increased PSD area on non-perforated mGluR-2/3^{+} synapses in the
346 Dutch mice.

347 Dutch mice showed altered presynaptic plasticity mechanisms related to the RRP of neurotransmitters.
348 Specifically, Dutch mice exhibited respectively faster rates of decay and recovery during high frequency
349 stimulation that causes fatigue at the synapses and after synaptic depression. The depletion and replenishment of
350 the RRP of neurotransmitters appear more profound in Dutch mice in comparison to wildtype mice. The RRP of
351 neurotransmitters refers to a small subset of neurotransmitter-containing vesicles residing close to the presynaptic
352 terminal (either docked or non-docked) and disposed for immediate released during stimulation. Besides
353 accumulation of Ca^{2+}, several parameters could affect the decay of the RRP including the number of active zones
354 and the number of docking sites at the presynaptic terminal. In turn, replenishment of the RRP could be mediated
355 by the Ca^{2+}-mediated recruitment of vesicles from the reserve pool to the RRP. The detailed mechanism of the
356 observed changes in the RRP of neurotransmitter requires further investigation.

357 The required interplay between pre- and postsynaptic neurons during synaptic plasticity suggests that
358 presynaptic changes could affect activation of postsynaptic neurons eventually leading to long-term synaptic
359 impairments. Despite the observed changes in the release probability and the RRP of neurotransmitters, high-
360 frequency stimulation resulted in normal LTP, suggesting that Dutch mice do not display derangement of
361 postsynaptic mechanisms at the ages studied, an observation that could be attributed to compensatory

362 mechanisms. In one possibility, the decrease in release probability with PTP may be balanced by the increased
363 depletion and replenishment of the RRP.

364 In contrast to previous reports, hippocampal microglia (Cluster 2) did not show a high number of DEGs, nor
365 were differences in expression of microglia DAM and homeostatic signatures observed between Dutch and
366 wildtype mice. The highest total and unique number of DEGs were found in excitatory neurons (Cluster 6) and
367 were associated with processes such as "protein translation" and "electron transport chain". Knowing that
368 presynaptic function can be impacted by oligodendrocytes(*38, 39*), and that Cluster 4 had the second highest total
369 number of DEGs, LR pairs were examined between oligodendrocytes and excitatory neurons, which indicated
370 that *Gabbr2* showed stronger interaction with multiple GABA inhibitory neurotransmitter complex partners in
371 Dutch mice.

372 Finally, prior studies using bulk RNAseq on the entorhinal cortex and dentate gyrus of wildtype and Dutch
373 mice were re-examined using scRNA-seq, revealing no obvious differences in microglial transcriptional profiles.
374 Moreover, the Dutch mouse hippocampal transcriptome did not present neuroinflammatory and microglial
375 transcriptomic responses that are commonly observed in models with senile plaques and amyloid fibrils (e.g.,
376 PSAPP, 5XFAD). Failure to capture such a response may be due to the cell populations selected for profiling.
377 Indeed, previous characterization indicated that microgliosis in other Dutch mice (*56*) was not generalized but
378 was limited to the immediate proximity of Aβ-laden vessels. In this study, no differences were observed in
379 microgliosis nor were increases detected in C1q colocalization with PSD95, a process reported to be induced by
380 NFA-Aβ, that drives activation of complement and synapse elimination(*35*). In a transcriptomic analysis on
381 postmortem brain tissue from humans with HCHWAD, inflammatory genes and pathways were also not
382 prominently represented(*57*). As detected in the Dutch mouse, the main pathways over-represented in the human
383 HCHWAD brains were related to mitochondrial dysfunction (*57*). The principal up-regulated pathways entail
384 interactions of the extracellular matrix and transforming growth factor beta signaling. In a clustering analysis to
385 identify molecular subtypes of AD, gene expression profiles have been gleaned from the Mount Sinai Brain Bank
386 (MSBB-AD) and Religious Orders Study-Memory and Aging Project (ROSMAP)(*58*). The Dutch mouse gene
387 signature significantly correlated with the subtype of "typical" or "Aβ predominant" AD presentation, and was
388 characterized by increased immune activation and inflammation, as well as decreased synaptic signaling and
389 dysregulation in neuronal processes and synaptic signaling (*58*). Considering our current results, the overlap
390 between the Dutch model and the AD subtypes may be more closely associated with alterations in synaptic
391 signaling than immune activation. Taken together, the results minimize the contribution of neuroinflammation in
392 the pathogenesis leading to learning disorder in Dutch mice.

393 Among the most dysregulated pathways in the Dutch mouse brain was "structural constituent of ribosome",
394 which is associated with the most significant GO term in Cluster 6 "protein translation". Increasing evidence

395 suggests that dysregulation of mRNA translation contributes to the pathogenesis of several neurological diseases,
396 including AD(*59*). Accumulation of Aβ is linked to increased protein synthesis through loss of interactions from
397 key translation regulators, particularly translation repressors(*60*). When the cell-type specific transcriptional
398 responses to NFA-Aβ were examined, altered transcriptional profiles were identified in multiple cell types. In
399 these profiles, overlap with GO term enrichment analysis indicated "amyloid-beta binding" among the shared
400 processes. Previously, both DEGs and processes altered in the Dutch mouse were identified in an aging-related
401 signature(*30*), and a recent study revealed that Aβ accumulation triggers fragmentation of the Golgi apparatus, a
402 key organelle needed for protein processing(*61*). A vicious cycle can be created because Golgi fragmentation
403 exacerbates Aβ production(*61*). On the contrary, prevention of the phosphorylation of Golgi structural proteins,
404 such as GRASP65, has rescued apparatus structure and reduced Aβ secretion(*61*).

405 The Cluster 6 neuron DEGs downregulated in Dutch mice compared to wildtype were associated with
406 mitochondrial functions, specifically GO terms "electron transport chain" and "oxidative phosphorylation". In
407 concordance, cellular respiration pathways were the most significantly altered pathways identified in the
408 transcriptomic analysis from human patients with HCHWAD(*57*). Moreover, fewer and smaller mitochondria
409 were found at the presynaptic terminals of excitatory neurons in the CA1 of Dutch mice compared to wildtype.
410 Strong evidence linking NFA-Aβ to mitochondrial complex I endpoints has come from the combined use of a
411 genetically encoded fluorescent redox sensor and multiphoton microscopy to image and monitor *in vivo* the
412 mitochondrial redox imbalance in neurons from the APP/PS1 transgenic mouse model of AD(*62*). The deposition
413 of Aβ plaque and particularly soluble NFA-Aβ species were shown to lead to increased mitochondrial oxidative
414 stress levels within neuronal mitochondria(*62*). Mitochondrial redox dysregulation in neurons was prevented by
415 inhibition of mitochondrial calcium influx, which is pathologically exacerbated in Aβ plaque-depositing mice(*62*).
416 Furthermore, mitochondria-targeting antioxidants decreased mitochondrial oxidative stress back to basal levels
417 and reverted Aβ plaque-associated dystrophic neurites in the APP/PS1 mice(*62*). Defective mitochondrial
418 complex I activity has been detected in living human AD brain(*63*). Altered mitochondrial fission and fusion has
419 been observed in the hippocampus of human AD and in Tg2576 mice and may explain the observations of
420 decreased mitochondrial density and smaller mitochondria in Dutch mice(*46, 65*). Increased mitochondrial
421 fragmentation has been reported in neurons exposed to NFA-Aβ(*66*). Elevated levels of NFA-Aβ impaired
422 transport of mitochondria in dendrites and axons and increased mitochondrial permeability in mice harboring the
423 Osaka mutation of APP (APP^{E693D})(*72*). Mitochondria-targeting therapy holds promise for treating
424 neurodegenerative disease (*108, 109*) and could be used in combination with other anti-Aβ and anti-tau therapies
425 to arrest AD progression. Our finding of reduced density of presynaptic mitochondria in the CA1 of Dutch mice
426 suggests that NFA-Aβ might also affect transport of mitochondria to axon terminals. The dysfunction of

427 mitochondria and endoplasmic reticulum (ER) protein translation observed in Dutch mice is consistent with
428 observations in other mouse models of AD(*62, 69*).

429 In conclusion, the current study provides several notable observations. Two independent methods visualized
430 for the first time *endogenously generated* NFA-Aβ *in vivo* in the absence of artefacts related to the intracerebral
431 injection of synthetic peptides or to the concurrent presence of Aβ fibrils. Changes related to the APP^{E693Q}-
432 genotype were revealed in NFA-Aβ histopathology, in expression of mitochondrial and neuronal translation-
433 related genes, in presynaptic physiology, and in the ultrastructure of presynaptic mitochondria.
434 Neuroinflammation is not a major contributor to the pathogenesis in Dutch mice. Neither fibrillar Aβ nor
435 neuroinflammation is required for the aging-related learning behavior phenotype.

436 This study of APP^{E693Q} mice is particularly timely considering the promising outcome of clinical trials for
437 lecanemab(*70*) and donanemab (*71*). Unlike other anti-amyloid antibodies, lecanemab selectively binds to NFA-
438 Aβ, leading to its neutralization and elimination(*70, 71*). After 18 months of treatment with either antibody,
439 participants experiencing mild cognitive impairment due to AD showed a modest but statistically significant 27%
440 slower rate of cognitive decline with lecanemab and 35% slower rate with donanemab. The modest clinical
441 response to therapeutic infusion of anti-amyloid antibodies may be attributable, at least in part, to the persistence
442 of residual toxic NFA-Aβ that goes undetected by current fluid biomarker analysis and amyloid fibril imaging.
443 The potential clinical importance of NFA-Aβ is reinforced by the recent discovery of a new FAD mutation
444 (APP^{D678N}) that also favors NFA-Aβ accumulation (*72*). Therapeutic depletion of NFA-Aβ may be required for
445 optimum and more robust cognitive benefits from anti-amyloid antibody infusion. Newer methods for imaging
446 NFA-Aβ (e.g., [^{64}Cu]-NOTA cyclic D,L-α-peptides) in the living human brain (*22*) and assays for detection of
447 NFA-Aβ in biofluids (*106, 107, 110*) may provide earlier diagnosis and improved monitoring of patients
448 undergoing Aβ immunodepletion therapy by assuring that both fibrillar and nonfibrillar Aβ conformers are
449 cleared as completely as possible.

450 **Materials and Methods**

451 *Experimental animals*

452 Male and female 2- to 24-month-old mice were used in this study. All animals were group housed in
453 microisolator cages under a 24-hour light/dark cycle and given *ad libitum* access to food and water. The Dutch
454 mice used in the study express the human *APP* gene harboring the Dutch mutation (APP^{E693Q}) under control of
455 the *Thy1* promoter(*18*). All animal procedures were conducted in accordance with the National Institute of Health
456 Guidelines for the Care and Use of Experimental Animals and were approved by the Institutional Animal Care
457 and Use Committees at the Icahn School of Medicine at Mount Sinai.

458 *Dot blot assay*

459 The cerebral cortices of mouse brain samples were thawed and lysed by adding 2x volume of lysis buffer
460 [5.0 mM NaCl, 5.0 mM EDTA, 1.0 mM dithiothreitol (DTT), and protease inhibitor mixture in 25 mM Tris
461 buffer, pH 7.5] containing 0.5 mm Zirconium Oxide Beads (ADV-ZrOBO5, ORNAT, Israel), homogenized with
462 a tissue grinder motor pestle (Alex-Red, Israel) on ice, and the mixtures were centrifuged at 4°C at 14,000 rpm
463 for 15 minutes. The total protein in each sample was quantified by Nano-Drop absorbance quantification at 280
464 nm.

465 For dot-blot analysis, equal amounts of samples of diluted proteins (100 ng/μL) were directly applied in
466 duplicate onto nitrocellulose membrane and dried at room temperature for 30 minutes. The membrane was then
467 blocked with 5% bovine serum albumin (BSA) in tris-buffered saline (TBS) (pH 7.4) containing 0.1% (v/v) Tween
468 20 (TBST). Blots were incubated overnight at 4°C with: 6E10 mouse monoclonal antibody (1:1000); rabbit
469 polyclonal antibody recognizing prefibrillar oligomers, A11 (1:5000); rabbit monoclonal antibody OC
470 recognizing fibrillar oligomers (1:1000); anti-murine-α-tubulin antibody (1:5000) in TBST containing 5% BSA.
471 The membranes were washed with TBST three times and incubated for 1 hour at room temperature with
472 horseradish peroxidase (HRP) conjugated either to an anti-mouse IgG (1:10000) or anti-rabbit IgG (1:5000) in
473 5% BSA in TBST. The blots were washed with TBST and developed using the enhanced chemiluminescence
474 (ECL) reagent kit (Pierce) in Amersham Imager 680 machine. Images were then used to analyze the mean of
475 integrated densities of each blot using ImageJ software (National Institutes of Health, USA)(*73*).

476 *Immunohistochemistry (IHC) and CP-2-FITC incubation*

477 All staining was performed in paraformaldehyde (PFA)-fixed 30 μm thick sections of Dutch and wildtype
478 mouse brains. For A11 immunohistochemistry and cyclic D,L-α-peptide-2 (CP-2)-FITC fluorescence, free-
479 floating sections were washed with 0.1 M phosphate buffer saline (PBS) in 0.1% Triton (PBST) three times for
480 15 minutes and blocked with 2% bovine serum albumin (BSA) for 1 hour. Sections were incubated with a rabbit
481 polyclonal antibody A11, recognizing Aβ prefibrillar oligomers (1:2500) in antibody buffer (PBST containing 2%
482 BSA) overnight at 4°C. Sections were washed and incubated with Alexa Fluor 680 secondary goat anti-rabbit
483 antibody (1:1000 Abcam) in antibody buffer for 1 hour at room temperature. Sections were then incubated with
484 fluorescein-5-isothiocyanate (FITC)-conjugated CP-2 [0.15 mg/mL in 2% dimethyl sulfoxide (DMSO)] for 3
485 hours at room temperature. Sections were washed for 10 min in 1% PBST and kept for 15 min to dry. Sections
486 were then mounted on super frost glass slides, embedded with Fluro-Gel II mounting medium containing DAPI
487 (4',6-diamidino-2-phenylindole dihydrochloride) (Electron Microscopy Sciences, Hatfield PA), cover-slipped,
488 and stored in the dark for microscopic imaging. Immunofluorescence images containing the hippocampus, cortex,
489 and thalamus were obtained using the 20x objective of a Leica DM6000 microscope (Leica Microsystems,
490 Wetzlar, Germany), coupled to a controller module and a high sensitivity 3CCD video camera system (MBF

491 Biosciences, VT) and an Intel Xeon workstation (Intel). All images were analyzed by the Image J program(*73*),
492 and one section from each mouse (from a total of 5 mice in each group) were taken for analysis. The average
493 intensity was calculated from the area of the hippocampus, cortex, and thalamus.

494 *Brain tissue homogenization and Aβ ELISAs*

495 Fresh frozen brain tissue (cerebrum) was homogenized at a 1:5 tissue:buffer ratio, using a Precellys Evolution
496 homogenizer (Bertin Technologies**,** Montigny-Le-Bretonneux, France) to sequentially extract TBS, TBS with
497 0.5% Triton X-100 (TBS-T) and formic acid (FA) soluble fractions of Aβ. After homogenization in TBS, samples
498 were centrifuged at 16,000× *g* for 1 h at 4 °C (TBS_{16K}). For a subset of experiments, a fraction of this supernatant
499 was further centrifuged at 100,000× *g* followed by collection of the supernatant (TBS_{100K}). Homogenization of
500 the remaining tissue pellet was repeated according to the same procedure with TBS-T, then followed by FA. Brain
501 extracts were analyzed with Aβ1-40 and Aβ1-42 ELISAs, as previously described(*74*). In brief, 96-well half-area
502 plates were coated over night with 50 ng/well of anti-Aβ40 (custom production, Agrisera) or anti-Aβ42 (700254,
503 Thermo Fisher Scientific, USA), then blocked with 1% BSA in PBS for 3 h at RT. TBS_{16K}, TBS-T and FA brain
504 extracts were diluted in ELISA incubation buffer (PBS, 0.1% BSA, 0.05% Tween) and incubated over night at 4
505 °C, followed by detection with 0.5 µg/ml biotinylated 3D6 and HRP-conjugated streptavidin (Mabtech AB,
506 Nacka, Sweden). Signals were developed with K Blue Aqueous TMB substrate (Neogen Corp., Lexington, KA,
507 US). Plates were developed and read with a spectrophotometer at 450 nm. The TBS and TBS-T extracts were also
508 analyzed for soluble Aβ aggregates using two different sandwich ELISAs. The first, based on 3D6 as both capture
509 and detection antibody, allows for detection of Aβ aggregates from the size of a dimer, but not for monomeric Aβ.
510 The second preferentially detects larger soluble Aβ aggregates as it utilizes the Aβ protofibril selective antibody
511 mAb158 for capture and 3D6 for detection(*75*). Ninety-six-well half-area plates were coated over night with 3D6
512 (50 ng/well) and blocked with 1% BSA in PBS for 3 h at RT. Brain extracts were diluted in ELISA incubation
513 buffer (PBS, 0.1% BSA, 0.05% Tween) and incubated over night at 4 °C, followed by 3D6biotin detection and
514 development as above.

515 *Slice preparation, electrophysiological recordings, and analysis*

516 For electrophysiological experiments, hippocampi from 7- to 13-month-old Dutch and wildtype mice were
517 excised on ice and coronal hippocampal slices (400 µm) were cut with a tissue chopper. Slices were transferred
518 to a recording chamber where they were allowed to recover for 2 hours at 29°C and perfused with artificial
519 cerebrospinal fluid (ACSF) containing (124.0 mM), KCl (4.4 mM), Na_2HPO_4 (1.0 mM), $NaHCO_3$ (25.0 mM),
520 $CaCl_2$ (2.0 mM), $MgCl_2$ (2.0 mM), and glucose (10.0 mM). ACSF was bubbled with carbogen (95% O_2 and 5%
521 CO_2) and perfused at a flow rate of 2 ml/minute.

522 Field excitatory post-synaptic potentials (fEPSP) were measured after stimulating the Schaffer collateral fibers
523 with a bipolar tungsten electrode placed at the CA3 and recording at the *stratum radiatum* of CA1 with a glass
524 pipette filled with ACSF. Basal synaptic transmission was evaluated by plotting the relationship between increased
525 voltages (5 V to 35 V) and evoked fEPSP responses, generating an input-output (I-O) curve. Recordings were
526 measured at approximately 35% of the maximum evoked response as determined by the I-O curve. For LTP
527 recordings, a 30-minute baseline was recorded prior to theta-burst stimulation (4 pulses at 100 Hz, with the bursts
528 repeated at 5 Hz and 3 tetani of 10-burst trains administered at 15-second intervals), responses were recorded for
529 2 hours after tetanization and measured as fEPSP slope expressed as percentage of baseline. Paired-pulse
530 facilitation (PPF) was induced by pairing two pulses at intervals of 15, 20, 30, 40, 50, 100, 200, 300, 500 and
531 1000 ms. PPF was expressed as the ratio between the second and the first fEPSP slopes. Post-tetanic potentiation
532 (PTP) was induced by the above-described theta-burst stimulation protocol in presence of the NMDA receptor
533 blocker D-APV (50 µM). Synaptic fatigue (SF) and replenishment were measured by 100 Hz stimulation followed
534 by 7 stimuli spaced at 125 msec from each other in the presence of D-APV (50 µM).
535 Results were analyzed in pClamp 11 (Molecular Devices) and fEPSP slopes were compared by 2-way ANOVA
536 for repeated measures for the I-O curve, LTP, PPF and PTP recordings. For statistical comparison of synaptic
537 fatigue and replenishment, the rates of exponential growth/decay (k) extra sum-of-squares F test was used to test
538 whether k differed between data sets vs. the data sets sharing one k-value. Statistics were performed using
539 GraphPad Prism 9 software. Data were expressed as mean ± SEM. The level of significance was set at $p<0.05$.

540 *Perfusions and tissue processing for electron microscopy and array tomography*

541 For electron microscopy (EM) and array tomography synapse studies, 12-month-old Dutch and wildtype mice
542 were anesthetized intraperitoneally, and transcardially perfused with 1% PFA in phosphate-buffered saline (PBS;
543 pH 7.4) followed by 4% PFA with 0.125% glutaraldehyde in PBS as described previously(*24, 76, 77*). The brains
544 were carefully removed, hemisected, postfixed overnight at 4°C in 4% PFA in PBS with 0.125% glutaraldehyde
545 for synapse and immunogold analyses, or by 2% PFA with 2% glutaraldehyde in PBS for presynaptic vesicle
546 analysis, and sectioned on a Vibratome (Leica VT1000S, Bannockburn, IL) into 250-µm thick sections. All
547 sections were stored at 4°C in PBS with 0.1% sodium azide until use. Coronal sections encompassing the CA1
548 region of the hippocampus were prepared for EM as reported(*24, 77*). For synapse and immunogold analyses,
549 slices were cryoprotected in graded phosphate buffer/glycerol washes at 4°C, and manually microdissected to
550 obtain blocks containing the CA1 region. The blocks were rapidly freeze-plunged into liquid propane cooled by
551 liquid nitrogen (-190°C) in a Universal cryofixation System KF80 (Reichert-Jung) and subsequently immersed in
552 1.5% uranyl acetate dissolved in anhydrous methanol at -90°C for 24 hours in a cryosubstitution unit (Leica).
553 Block temperatures were raised from -90°C to -45°C in steps of 4°C/hour, washed with anhydrous methanol, and
554 infiltrated with Lowicryl resin (Electron Microscopy Sciences) at -45°C. The resin was polymerized by exposure

555 to ultraviolet light (360 nm) for 48 hours at -45°C followed by 24 hours at 0°C. For presynaptic vesicle studies,
556 tissue blocks were washed overnight in 0.1 M sodium cacodylate buffer, placed in 1% tannic acid/0.1 M
557 cacodylate buffer solution at room temperature for one hour and washed 3 times for 10 minutes each in 0.1 M
558 sodium cacodylate. The samples were then incubated for 1 hour at room temperature in 2% osmium
559 tetroxide/double distilled water (ddH_2O), washed again in 0.1 M sodium cacodylate 3 times for 10 minutes then
560 subjected to a graduated ethanol dehydration series. After dehydration, the tissue samples were infiltrated with
561 Spurr Low Viscosity Embedding Kit (Sigma Aldrich) and polymerized for 12 hours at 70°C. For both EM
562 preparations, block faces were trimmed, ultrathin sections (90 nm) were cut with a diamond knife (Diatome) on
563 an ultramicrotome (Reichert-Jung), and sections were collected on formvar/carbon-coated nickel slot grids
564 (Electron Microscopy Sciences).

565 *Post-embedding immunogold labeling for EM*

566 Immuno-gold labeling was performed using a previously optimized method(*78*). Briefly, the EM sections were
567 treated with 0.1% sodium borohydride in 50 mM glycine prepared in Tris buffer for 6 minutes in the dark, to
568 remove aldehydes. Sections were then subjected to six quick rinses and two 10-minute washes in TBS. The
569 sections were incubated for 30 min in blocking buffer consisting of 2% human serum albumin (HSA) in TBS with
570 0.1% Triton X-100. After three short washes in TBS, the sections were incubated in anti-glutamate receptor 2 &
571 3 rabbit polyclonal antibody (Millipore AB1506, diluted 1:100 in 2% HSA in TBS) at room temperature overnight
572 with gentle shaking. Following six quick rinses and two 5-minute washes in TBS, the grids were incubated in
573 blocking buffer for 20 minutes, washed three times, and incubated for 90 minutes at room temperature in goat
574 anti-rabbit IgG conjugated to 10-nm gold particles (Aurion 25362), diluted 1:40 in 2% HSA and 5 mg/ml
575 polyethylene glycol in TBS. The grids were rinsed six times and washed for 5 minutes in TBS and then in
576 deionized water. Imaging was done using an H-7000 electron microscope (Hitachi High Technologies America,
577 Inc.) with an AMT Advantage CCD camera (Advanced Microscopy Techniques) at 15,000x. The electron
578 micrographs were adjusted for brightness and sharpness with Photoshop CS5 (Adobe Systems).

579 *Quantifying synapse density, ultrastructure, and distribution of immunogold particles at mGluR-2/3-labeled*
580 *synapses*

581 All EM analyses were conducted by an experimenter blinded to the genotypes of the mice. For synapse
582 quantification and ultrastructural analysis, nine sets of serial images across the same set of 5 consecutive ultrathin
583 sections were taken from the *stratum radiatum* of CA1 and imported into Adobe Photoshop (version CS5). To
584 obtain a stereologically unbiased population of synapses for quantitative morphologic analysis, we used a disector
585 approach on ultrathin sections as described(*24, 76, 77, 79*). Briefly, all axospinous synapses were identified within
586 the first and last 2 images of each 5-section serial set and counted if they were contained in the reference image

587 (layers 1 and 4) but not in the corresponding look-up image (layers 2 and 5). To increase sampling efficiency, the
588 reference image and look-up image were then reversed; thus, each animal included in the current study contributed
589 synapse density data from a total of 18 disector pairs. The total volume examined was 11.317 μm^3, and the height
590 of the disector was 180 nm. Axospinous synapse density (per μm^3) was calculated as the total number of counted
591 synapses from both images divided by the total volume of the disector. The criteria for inclusion as an axospinous
592 synapse included the presence of synaptic vesicles in the presynaptic terminal and a distinct asymmetric PSD
593 separated by a clear synaptic cleft. For a synapse to be scored as perforated it had to display two or more separate
594 PSDs.

595 To measure structural parameters such as spine head diameter and PSD length, we identified all axospinous
596 synapses in the middle portion of three serial sections. The synapse and spine head were followed through layers
597 2-5. In each layer, the PSD length (if present) and the spine head diameter at its widest point parallel to the synapse
598 were measured. PSD area was determined by summing the PSD lengths through all sections and multiplying by
599 section thickness (90 μm). This same process was repeated for unique synapses in layer 4 (reference layer 5),
600 following the synapses from layer 4 to layer 1. Each of these synapses were also classified as non-perforated or
601 perforated. A total of 734 total synapses (341 from Dutch mice and 393 from wildtype) were analyzed in this
602 manner. An average of 81 synapses per animal and a minimum of 71 synapses per animal were sampled. For each
603 unique synapse in layer 2 in each series (as identified for PSD length and spine head analysis above), the synapse
604 was followed through layers 2 though 5 and the number of immunogold particles in each of the following areas
605 were counted: active zone (presynaptic, within 45 nm of the membrane across from the PSD; region A), synaptic
606 cleft (region B), PSD (region C), peri-synaptic (peri—PSD, within 200 nm of the PSD on the post-synaptic spine
607 head; region D), postsynaptic membrane (>200 nm away from the PSD; region E), and postsynaptic cytoplasm
608 (region F). A cutoff of 45 nm away from the membrane was used to differentiate between receptors at the
609 membrane and receptors in the cytosol.

610 For presynaptic vesicle analysis, 100 synapses per animal were analyzed from at least 30 different images
611 taken at a magnification of 8,000x. PSD length, maximum spine head diameter, and cytosolic area of the
612 presynaptic terminal were measured using Adobe Photoshop 2023. Vesicles in the presynaptic terminal were
613 labeled with a dot in the center of the vesicle, and a line was drawn over the PSD. An algorithm was written in
614 Python that measured the shortest distance between each vesicle (represented by the dot in the center) and its
615 corresponding PSD (represented by the manually drawn line over the PSD) and reported a list of measurements
616 for all vesicles within an adjustable threshold distance (**Supplemental Figure 5**). For each synapse, the total
617 number of vesicles was determined with output from this algorithm, along with their individual distances from
618 the PSD. The vesicles were divided into bins of 10 and 50 nm for comparison of spatial distribution within the

presynaptic terminal. Additionally, vesicles within 10 nm of the PSD were classified as docked, based on a 17 nm average minimum diameter of vesicles in our samples(*80-82*).

ScRNA-seq and data analysis

For the scRNA-seq experiments, fresh hippocampi were dissected from 12- to 13-month-old Dutch and wildtype mice, and the tissue was dissociated into a single-cell suspension following the 10X Genomics sample preparation protocol. We pooled the hippocampi from 3 mice of the same gender, genotype, and age to reach the target concentration of 2000 cells/µl. The single cell cDNA libraries were generated using a V3 Chromium kit (10X Genomics) and sequenced using a NovaSeq S4 (Illumina).

The raw sequencing data were processed using the standard Cell Ranger pipeline to generate unique molecular identifier (UMI) count matrices. Starting from UMI matrices, we first performed quality control (QC) by removing low-quality cells with either too few (< 200) or too many (> 4000) genes detected, retaining 61,642 cells after filtering. We then removed insufficiently detected genes by keeping 20,548 genes expressed in more than one cell. After QC, we obtained 5,266 ~ 10,949 cells per individual, and an average of 618 unique genes per cell per individual. We performed a clustering analysis using a well-established scRNA-seq data integration workflow based on R package Seurat (v3)(*83*). Briefly, the UMIs data were first normalized by sequencing depth and log-transformed using the LogNormalize method implemented in Seurat. The 2,000 most variable gene features were identified, scaled, and centered. The scRNA-seq data across all sequencing libraries were combined based on the canonical correlation analysis (CCA) integration method available from Seurat. Next, dimensional reduction was performed using principal component analysis (PCA) based on the 2,000 most variable genes. The top 25 principal components (PCs) collectively explaining more than 90% of the variance were selected for calculating 2D dimensional reductions by Uniform Manifold Approximation and Projection for Dimension Reduction (UMAP)(*84*). The same top 25 PCs were also used to compute the nearest neighbor graph and the subsequent cell clusters with the Louvain algorithm implemented in Seurat (*83*). This clustering analysis resulted in 14 clusters (named as Clusters 0 – 13, sorted by cluster size in a decreasing order) at a clustering resolution of 0.1. These clusters contained 267 to 20,702 cells each.

Cluster cell type annotation

For each cluster, we first interrogated the expression patterns of known gene markers to annotate clusters into major cell-types: inhibitory neurons (*Gad1*, *Gad2*), excitatory neurons (*Slc17a7*), astrocytes (*Aqp4*), oligodendrocytes (*Mog*), microglia (*Csf1r*, *Tyrobp,* and *Trem2*), oligodendrocyte progenitor cells (*Vcan* and *Pdgfra*), endothelial cells (*Flt1*), and pericytes (*Vtn* and *Pdgfrb*). Next, we calculated *de novo* cluster signatures by comparing the cells in a cluster against the cells of the other clusters using Wilcoxon rank sum test in Seurat. We defined cluster marker genes as those upregulated by at least 1.2-fold and with Bonferroni adjusted p-value less than 0.05. To assist the annotation of cell type of each cluster, we overlapped the *de novo* cluster marker gene

652 signatures with a large-scale collection of cell type markers curated from over 1,054 single-cell experiments(*85*),
653 with p-value significance of the overlaps computed by a hypergeometric test.

654 *Cluster-specific differential gene expression and functional enrichment analysis*

655 DEGs between Dutch and wild type sample groups in each cluster were identified using MAST(*86, 87*)
656 implemented in Seurat. Similarly, DEGs between males and females, and DEGs between Dutch and wild type in
657 each sex group were identified using MAST. DEGs were determined at the cutoff of Bonferroni-corrected p-value
658 $\leq$ 0.05. Functional enrichment of DEGs with MSigDB gene annotation collections was examined by a
659 hypergeometric test. Results with Benjamini-Hochberg (BH) correction p-value $\leq$ 0.05 were considered
660 statistically significant.

661 *Microglia subclustering analysis*

662 We studied a subset of microglial cells from the full data matrix. PCA was performed and then the top PCs
663 collectively explaining more than 90% of the variance were selected for calculating dimensional reduction by
664 UMAP (*84*) as well as for clustering analysis using Seurat (*83*). To test if the microglia subclusters represent
665 known subtypes, we computed single cell signature scores (*88*) corresponding to homeostatic, disease-associated
666 microglia (DAM), type I IFN-induced (IFN) and MHC-expressing (MHC) microglia based on signature genes
667 curated by Chen and Colonna (*34*).

668 *Quantifying presynaptic mitochondrial numbers and morphology*

669 For analysis of mitochondria, 12 series of 9 consecutive 90-nm thick sections were selected from each mouse
670 using a systematic-random approach for EM imaging. All mitochondrial analyses were performed by the same
671 experimenter, blinded to the group designation of subjects as described (*89*). For each series of 9 consecutive
672 sections, the middle fifth section was used as a reference, and all pre-synaptic axonal boutons containing a
673 mitochondrion were identified. Each of these boutons was followed throughout the series, and the number, length
674 and morphology of mitochondria were recorded. Mitochondria were classified as either straight or curved.
675 Mitochondria that were bent at least 90° were identified as curved, while all other mitochondria were classified
676 as straight.

677 *Statistics*

678 Data sets from the dot blot assays were analyzed using a one-way ANOVA followed by Tukey's multiple
679 comparisons test. Data sets from the A11 immunohistochemistry and CP-2 cyclic peptide-FITC (CP-2-FITC) (*22*)
680 fluorescence microscopy were analyzed using a two-way ANOVA followed by Sidak's multiple comparisons test.
681 Data sets were analyzed using a two-tailed Student's t-test. Threshold for significance was set at $\alpha = 0.05$.
682 Distribution of mGluR-2/3 immunogold particles was analyzed using repeated measures ANOVA. Data are

683 represented as mean ± SD. Statistical analyses were carried out using Prism software (version 9.2.0, GraphPad
684 Software, San Diego, CA).

685 *Data Availability*

686 The scRNA-seq data (cell ranger processed count matrices) are in a Synapse repository (accession
687 syn52752404, with direct link https://www.synapse.org/#!Synapse:syn52752404/files/).

688 **References**

689 1. S. W. Scheff, D. A. Price, F. A. Schmitt, S. T. DeKosky, E. J. Mufson. Synaptic alterations in CA1 in mild Alzheimer
690 disease and mild cognitive impairment. *Neurology* **68**, 1501-1508 (2007).
691 2. T. Arendt, Synaptic degeneration in Alzheimer's disease. *Acta Neuropathol* **118**, 167-179 (2009).
692 3. G. M. Shankar, D. M. Walsh. Alzheimer's disease: synaptic dysfunction and Abeta. *Mol Neurodegener* **4**, 48 (2009).
693 4. A. John, P. H. Reddy. Synaptic basis of Alzheimer's disease: Focus on synaptic amyloid beta, P-tau and
694 mitochondria. *Ageing Res Rev* **65**, 101208 (2021).
695 5. M. Pang, L. Zhu, A. Gabelle, A. R. Gafson, R. W. Platt, J. E. Galvin, P. Krolak-Salmon, I. Rubino, C. de Moor, S.
696 Belachew, C. Shen. Effect of reduction in brain amyloid levels on change in cognitive and functional decline in
697 randomized clinical trials: An instrumental variable meta-analysis. *Alzheimers Dement*, (2022).
698 6. T. Bussiere, P. D. Friend, N. Sadeghi, B. Wicinski, G. I. Lin, C. Bouras, P. Giannakopoulos, N. K. Robakis, J. H.
699 Morrison, D. P. Perl, P. R. Hof. Stereologic assessment of the total cortical volume occupied by amyloid deposits
700 and its relationship with cognitive status in aging and Alzheimer's disease. *Neuroscience* **112**, 75-91 (2002).
701 7. A. Akram, D. Christoffel, A. B. Rocher, C. Bouras, E. Kovari, D. P. Perl, J. H. Morrison, F. R. Herrmann, V.
702 Haroutunian, P. Giannakopoulos, P. R. Hof. Stereologic estimates of total spinophilin-immunoreactive spine number
703 in area 9 and the CA1 field: relationship with the progression of Alzheimer's disease. *Neurobiol Aging* **29**, 1296-
704 1307 (2008).
705 8. P. T. Nelson, I. Alafuzoff, E. H. Bigio, C. Bouras, H. Braak, N. J. Cairns, R. J. Castellani, B. J. Crain, P. Davies,
706 K. Del Tredici, C. Duyckaerts, M. P. Frosch, V. Haroutunian, P. R. Hof, C. M. Hulette, B. T. Hyman, T. Iwatsubo,
707 K. A. Jellinger, G. A. Jicha, E. Kövari, W. A. Kukull, J. B. Leverenz, S. Love, I. R. Mackenzie, D. M. Mann, E.
708 Masliah, A. C. McKee, T. J. Montine, J. C. Morris, J. A. Schneider, J. A. Sonnen, D. R. Thal, J. Q. Trojanowski, J.
709 C. Troncoso, T. Wisniewski, R. L. Woltjer, T. G. Beach. Correlation of Alzheimer disease neuropathologic changes
710 with cognitive status: a review of the literature. *J Neuropathol Exp Neurol* **71**, 362-381 (2012).
711 9. K. Ishibashi, T. Tomiyama, K. Nishitsuji, M. Hara, H. Mori. Absence of synaptophysin near cortical neurons
712 containing oligomeric Abeta in Alzheimer's disease brain. *J Neurosci Res* **84**, 632-636 (2006).
713 10. M. P. Lambert, A. K. Barlow, B. A. Chromy, C. Edwards, R. Freed, M. Liosatos, T. E. Morgan, I. Rozovsky, B.
714 Trommer, K. L. Viola, P. Wals, C. Zhang, C. E. Finch, G. A. Krafft, W. L. Klein. Diffusible, nonfibrillar ligands
715 derived from Abeta1-42 are potent central nervous system neurotoxins. *Proc Natl Acad Sci U S A* **95**, 6448-6453
716 (1998).
717 11. J. A. Fein, S. Sokolow, C. A. Miller, H. V. Vinters, F. Yang, G. M. Cole, K. H. Gylys. Co-localization of amyloid
718 beta and tau pathology in Alzheimer's disease synaptosomes. *Am J Pathol* **172**, 1683-1692 (2008).
719 12. S. Sokolow, K. M. Henkins, T. Bilousova, C. A. Miller, H. V. Vinters, W. Poon, G. M. Cole, K. H. Gylys. AD
720 synapses contain abundant Abeta monomer and multiple soluble oligomers, including a 56-kDa assembly.
721 *Neurobiol Aging* **33**, 1545-1555 (2012).
722 13. T. Bilousova, C. A. Miller, W. W. Poon, H. V. Vinters, M. Corrada, C. Kawas, E. Y. Hayden, D. B. Teplow, C. Glabe,
723 R. Albay, 3rd, G. M. Cole, E. Teng, K. H. Gylys. Synaptic Amyloid-beta Oligomers Precede p-Tau and Differentiate
724 High Pathology Control Cases. *Am J Pathol* **186**, 185-198 (2016).
725 14. D. M. Walsh, I. Klyubin, J. V. Fadeeva, W. K. Cullen, R. Anwyl, M. S. Wolfe, M. J. Rowan, D. J. Selkoe. Naturally
726 secreted oligomers of amyloid beta protein potently inhibit hippocampal long-term potentiation in vivo. *Nature* **416**,
727 535-539 (2002).
728 15. G. M. Shankar, B. L. Bloodgood, M. Townsend, D. M. Walsh, D. J. Selkoe, B. L. Sabatini. Natural oligomers of the
729 Alzheimer amyloid-beta protein induce reversible synapse loss by modulating an NMDA-type glutamate receptor-
730 dependent signaling pathway. *J Neurosci* **27**, 2866-2875 (2007).

16. J. P. Cleary, D. M. Walsh, J. J. Hofmeister, G. M. Shankar, M. A. Kuskowski, D. J. Selkoe, K. H. Ashe. Natural oligomers of the amyloid-beta protein specifically disrupt cognitive function. *Nat Neurosci* **8**, 79-84 (2005).
17. B. DaRocha-Souto, T. C. Scotton, M. Coma, A. Serrano-Pozo, T. Hashimoto, L. Sereno, M. Rodriguez, B. Sanchez, B. T. Hyman, T. Gomez-Isla. Brain oligomeric beta-amyloid but not total amyloid plaque burden correlates with neuronal loss and astrocyte inflammatory response in amyloid precursor protein/tau transgenic mice. *J Neuropathol Exp Neurol* **70**, 360-376 (2011).
18. S. Gandy, A. J. Simon, J. W. Steele, A. L. Lublin, J. J. Lah, L. C. Walker, A. I. Levey, G. A. Krafft, E. Levy, F. Checler, C. Glabe, W. B. Bilker, T. Abel, J. Schmeidler, M. E. Ehrlich. Days to criterion as an indicator of toxicity associated with human Alzheimer amyloid-beta oligomers. *Ann Neurol* **68**, 220-230 (2010).
19. E. Levy, M. D. Carman, I. J. Fernandez-Madrid, M. D. Power, I. Lieberburg, S. G. van Duinen, G. T. Bots, W. Luyendijk, B. Frangione. Mutation of the Alzheimer's disease amyloid gene in hereditary cerebral hemorrhage, Dutch type. *Science* **248**, 1124-1126 (1990).
20. M. L. Maat-Schieman, S. G. van Duinen, J. Haan, R. A. Roos. Morphology of cerebral plaque-like lesions in hereditary cerebral hemorrhage with amyloidosis (Dutch). *Acta Neuropathol* **84**, 674-679 (1992).
21. E. M. Knight, S. H. Kim, J. C. Kottwitz, A. Hatami, R. Albay, A. Suzuki, A. Lublin, C. M. Alberini, W. L. Klein, P. Szabo, N. R. Relkin, M. Ehrlich, C. G. Glabe, S. Gandy, J. W. Steele. Effective anti-Alzheimer Abeta therapy involves depletion of specific Abeta oligomer subtypes. *Neurol Neuroimmunol Neuroinflamm* **3**, e237 (2016).
22. M. Habashi, S. Vutla, K. Tripathi, S. Senapati, P. S. Chauhan, A. Haviv-Chesner, M. Richman, S.-A. Mohand, V. Dumulon-Perreault, R. Mulamreddy, E. Okun, J. H. Chill, B. Guérin, W. D. Lubell, S. Rahimipour. Early diagnosis and treatment of Alzheimer's disease by targeting toxic soluble Aβ oligomers. *Proceedings of the National Academy of Sciences* **119**, e2210766119 (2022).
23. G. Kaur, M. Pawlik, S. E. Gandy, M. E. Ehrlich, J. F. Smiley, E. Levy. Lysosomal dysfunction in the brain of a mouse model with intraneuronal accumulation of carboxyl terminal fragments of the amyloid precursor protein. *Mol Psychiatry* **22**, 981-989 (2017).
24. K. A. Price, M. Varghese, A. Sowa, F. Yuk, H. Brautigam, M. E. Ehrlich, D. L. Dickstein,.Altered synaptic structure in the hippocampus in a mouse model of Alzheimer's disease with soluble amyloid-beta oligomers and no plaque pathology. *Mol Neurodegener* **9**, 41 (2014).
25. B. Readhead, J. V. Haure-Mirande, B. Zhang, V. Haroutunian, S. Gandy, E. E. Schadt, J. T. Dudley, M. E. Ehrlich. Molecular systems evaluation of oligomerogenic APP(E693Q) and fibrillogenic APP(KM670/671NL)/PSEN1(Deltaexon9) mouse models identifies shared features with human Alzheimer's brain molecular pathology. *Mol Psychiatry* **21**, 1153-1154 (2016).
26. S. Tucker, C. Möller, K. Tegerstedt, A. Lord, H. Laudon, J. Sjödahl, L. Söderberg, E. Spens, C. Sahlin, E. R. Waara, A. Satlin, P. Gellerfors, G. Osswald, L. Lannfelt. The murine version of BAN2401 (mAb158) selectively reduces amyloid-β protofibrils in brain and cerebrospinal fluid of tg-ArcSwe mice. *J Alzheimers Dis* **43**, 575-588 (2015).
27. R. S. Zucker, W. G. J. A. r. o. p. Regehr. Short-term synaptic plasticity. **64**, 355-405 (2002).
28. H. Zhang, B. Gong, S. Liu, M. Fa, I. Ninan, A. Staniszewski, O. J. C. A. R. Arancio. Synaptic fatigue is more pronounced in the APP/PS1 transgenic mouse model of Alzheimer's disease. **2**, 137-140 (2005).
29. G. Yu, L.-G. Wang, Y. Han, Q.-Y. He, clusterProfiler: an R Package for Comparing Biological Themes Among Gene Clusters. *OMICS: A Journal of Integrative Biology* **16**, 284-287 (2012).
30. M. Ximerakis, S. L. Lipnick, B. T. Innes, S. K. Simmons, X. Adiconis, D. Dionne, B. A. Mayweather, L. Nguyen, Z. Niziolek, C. Ozek, V. L. Butty, R. Isserlin, S. M. Buchanan, S. S. Levine, A. Regev, G. D. Bader, J. Z. Levin, L. Rubin. Single-cell transcriptomic profiling of the aging mouse brain. *Nature Neuroscience* **22**, 1696-1708 (2019).
31. S. Krasemann, C. Madore, R. Cialic, C. Baufeld, N. Calcagno, R. El Fatimy, L. Beckers, E. O'Loughlin, Y. Xu, Z. Fanek, D. J. Greco, S. T. Smith, G. Tweet, Z. Humulock, T. Zrzavy, P. Conde-Sanroman, M. Gacias, Z. Weng, H. Chen, E. Tjon, F. Mazaheri, K. Hartmann, A. Madi, J. D. Ulrich, M. Glatzel, A. Worthmann, J. Heeren, B. Budnik, C. Lemere, T. Ikezu, F. L. Heppner, V. Litvak, D. M. Holtzman, H. Lassmann, H. L. Weiner, J. Ochando, C. Haass, O. Butovsky. The TREM2-APOE Pathway Drives the Transcriptional Phenotype of Dysfunctional Microglia in Neurodegenerative Diseases. *Immunity* **47**, 566-581.e569 (2017).
32. G. D. Manocha, A. M. Floden, K. Rausch, J. A. Kulas, B. A. McGregor, L. Rojanathammanee, K. R. Puig, K. L. Puig, S. Karki, M. R. Nichols, D. C. Darland, J. E. Porter, C. K. Combs. APP Regulates Microglial Phenotype in a Mouse Model of Alzheimer's Disease. *J Neurosci* **36**, 8471-8486 (2016).

33. H. Keren-Shaul, A. Spinrad, A. Weiner, O. Matcovitch-Natan, R. Dvir-Szternfeld, T. K. Ulland, E. David, K. Baruch, D. Lara-Astaiso, B. Toth, S. Itzkovitz, M. Colonna, M. Schwartz, I. Amit. A Unique Microglia Type Associated with Restricting Development of Alzheimer's Disease. *Cell* **169**, 1276-1290.e1217 (2017).
34. Y. Chen, M. Colonna. Microglia in Alzheimer's disease at single-cell level. Are there common patterns in humans and mice? *J Exp Med* **218**, (2021).
35. S. Hong, V. F. Beja-Glasser, B. M. Nfonoyim, A. Frouin, S. Li, S. Ramakrishnan, K. M. Merry, Q. Shi, A. Rosenthal, B. A. Barres, C. A. Lemere, D. J. Selkoe, B. Stevens. Complement and microglia mediate early synapse loss in Alzheimer mouse models. *Science* **352**, 712-716 (2016).
36. P. Sunderaraman, S. Cosentino, N. Schupf, J. Manly, Y. Gu, S. Barral. MEF2C Common Genetic Variation Is Associated With Different Aspects of Cognition in Non-Hispanic White and Caribbean Hispanic Non-demented Older Adults. *Front Genet* **12**, 642327 (2021).
37. J. C. Lambert, C. A. Ibrahim-Verbaas, D. Harold, A. C. Naj, R. Sims, C. Bellenguez, A. L. DeStafano, J. C. Bis, G. W. Beecham, B. Grenier-Boley, G. Russo, T. A. Thorton-Wells, N. Jones, A. V. Smith, V. Chouraki, C. Thomas, M. A. Ikram, D. Zelenika, B. N. Vardarajan, Y. Kamatani, C. F. Lin, A. Gerrish, H. Schmidt, B. Kunkle, M. L. Dunstan, A. Ruiz, M. T. Bihoreau, S. H. Choi, C. Reitz, F. Pasquier, C. Cruchaga, D. Craig, N. Amin, C. Berr, O. L. Lopez, P. L. De Jager, V. Deramecourt, J. A. Johnston, D. Evans, S. Lovestone, L. Letenneur, F. J. Morón, D. C. Rubinsztein, G. Eiriksdottir, K. Sleegers, A. M. Goate, N. Fiévet, M. W. Huentelman, M. Gill, K. Brown, M. I. Kamboh, L. Keller, P. Barberger-Gateau, B. McGuiness, E. B. Larson, R. Green, A. J. Myers, C. Dufouil, S. Todd, D. Wallon, S. Love, E. Rogaeva, J. Gallacher, P. St George-Hyslop, J. Clarimon, A. Lleo, A. Bayer, D. W. Tsuang, L. Yu, M. Tsolaki, P. Bossù, G. Spalletta, P. Proitsi, J. Collinge, S. Sorbi, F. Sanchez-Garcia, N. C. Fox, J. Hardy, M. C. Deniz Naranjo, P. Bosco, R. Clarke, C. Brayne, D. Galimberti, M. Mancuso, F. Matthews, S. Moebus, P. Mecocci, M. Del Zompo, W. Maier, H. Hampel, A. Pilotto, M. Bullido, F. Panza, P. Caffarra, B. Nacmias, J. R. Gilbert, M. Mayhaus, L. Lannefelt, H. Hakonarson, S. Pichler, M. M. Carrasquillo, M. Ingelsson, D. Beekly, V. Alvarez, F. Zou, O. Valladares, S. G. Younkin, E. Coto, K. L. Hamilton-Nelson, W. Gu, C. Razquin, P. Pastor, I. Mateo, M. J. Owen, K. M. Faber, P. V. Jonsson, O. Combarros, M. C. O'Donovan, L. B. Cantwell, H. Soininen, D. Blacker, S. Mead, T. H. Mosley, Jr., D. A. Bennett, T. B. Harris, L. Fratiglioni, C. Holmes, R. F. de Bruijn, P. Passmore, T. J. Montine, K. Bettens, J. I. Rotter, A. Brice, K. Morgan, T. M. Foroud, W. A. Kukull, D. Hannequin, J. F. Powell, M. A. Nalls, K. Ritchie, K. L. Lunetta, J. S. Kauwe, E. Boerwinkle, M. Riemenschneider, M. Boada, M. Hiltuenen, E. R. Martin, R. Schmidt, D. Rujescu, L. S. Wang, J. F. Dartigues, R. Mayeux, C. Tzourio, A. Hofman, M. M. Nöthen, C. Graff, B. M. Psaty, L. Jones, J. L. Haines, P. A. Holmans, M. Lathrop, M. A. PericakVance, L. J. Launer, L. A. Farrer, C. M. van Duijn, C. Van Broeckhoven, V. Moskvina, S. Seshadri, J. Williams, G. D. Schellenberg, P. Amouyel. Meta-analysis of 74,046 individuals identifies 11 new susceptibility loci for Alzheimer's disease. *Nat Genet* **45**, 1452-1458 (2013).
38. M. Jang, E. Gould, J. Xu, E. J. Kim, J. H. Kim. Oligodendrocytes regulate presynaptic properties and neurotransmission through BDNF signaling in the mouse brainstem. *Elife* **8**, (2019).
39. C. Habermacher, M. C. Angulo, N. Benamer. Glutamate versus GABA in neuron-oligodendroglia communication. *Glia* **67**, 2092-2106 (2019).
40. K. Hoshi, H. Ito, E. Abe, T. J. Fuwa, M. Kanno, Y. Murakami, M. Abe, T. Murakami, A. Yoshihara, Y. Ugawa, T. Saito, T. C. Saido, K. Matsumoto, Y. Yamaguchi, K. Furukawa, H. Arai, M. Kanai, M. Miyajima, H. Arai, N. Ogawa, H. Akatsu, Y. Hashizume, H. Tateno, T. Honda, Y. Hashimoto. Transferrin Biosynthesized in the Brain Is a Novel Biomarker for Alzheimer's Disease. *Metabolites* **11**, (2021).
41. N. Lemon, E. Canepa, M. A. Ilies, S. Fossati. Carbonic Anhydrases as Potential Targets Against Neurovascular Unit Dysfunction in Alzheimer's Disease and Stroke. *Front Aging Neurosci* **13**, 772278 (2021).
42. X. Wang, B. E. Figueroa, I. G. Stavrovskaya, Y. Zhang, A. C. Sirianni, S. Zhu, A. L. Day, B. S. Kristal, R. M. Friedlander. Methazolamide and melatonin inhibit mitochondrial cytochrome C release and are neuroprotective in experimental models of ischemic injury. *Stroke* **40**, 1877-1885 (2009).
43. A. Lee, C. Kondapalli, D. M. Virga, T. L. Lewis, Jr., S. Y. Koo, A. Ashok, G. Mairet-Coello, S. Herzig, M. Foretz, B. Viollet, R. Shaw, A. Sproul, F. Polleux. Aβ42 oligomers trigger synaptic loss through CAMKK2-AMPKdependent effectors coordinating mitochondrial fission and mitophagy. *Nat Commun* **13**, 4444 (2022).
44. B. A. Györffy, V. Tóth, G. Török, P. Gulyássy, R. Kovács, H. Vadászi, A. Micsonai, M. E. Tóth, M. Sántha, L. Homolya, L. Drahos, G. Juhász, K. A. Kékesi, J. Kardos. Synaptic mitochondrial dysfunction and septin

833 accumulation are linked to complement-mediated synapse loss in an Alzheimer's disease animal model. *Cell Mol*
834 *Life Sci* **77**, 5243-5258 (2020).
835 45. A. Norambuena, H. Wallrabe, R. Cao, D. B. Wang, A. Silva, Z. Svindrych, A. Periasamy, S. Hu, R. E. Tanzi, D. Y.
836 Kim, G. S. Bloom, A novel lysosome-to-mitochondria signaling pathway disrupted by amyloid-β oligomers. *The*
837 *EMBO Journal* **37**, e100241 (2018).
838 46. M. J. Calkins, M. Manczak, P. Mao, U. Shirendeb, P. H. Reddy. Impaired mitochondrial biogenesis, defective axonal
839 transport of mitochondria, abnormal mitochondrial dynamics and synaptic degeneration in a mouse model of
840 Alzheimer's disease. *Hum Mol Genet* **20**, 4515-4529 (2011).
841 47. J. S. da Silva, Y. Nonose, F. Rohden, P. C. Lukasewicz Ferreira, F. U. Fontella, A. Rocha, A. W. Brochier, R. V.
842 Apel, T. M. de Lima, B. Seminotti, A. U. Amaral, A. Galina, D. O. Souza. Guanosine Neuroprotection of Presynaptic
843 Mitochondrial Calcium Homeostasis in a Mouse Study with Amyloid-beta oligomers. *Mol Neurobiol* **57**, 4790-
844 4809 (2020).
845 48. I. Klyubin, D. M. Walsh, W. K. Cullen, J. V. Fadeeva, R. Anwyl, D. J. Selkoe, M. J. Rowan. Soluble Arctic amyloid
846 beta protein inhibits hippocampal long-term potentiation in vivo. *Eur J Neurosci* **19**, 2839-2846 (2004).
847 49. R. Janz, T. C. Südhof, R. E. Hammer, V. Unni, S. A. Siegelbaum, V. Y. J. N. Bolshakov. Essential roles in synaptic
848 plasticity for synaptogyrin I and synaptophysin I. **24**, 687-700 (1999).
849 50. W. Q. Zhao, F. Santini, R. Breese, D. Ross, X. D. Zhang, D. J. Stone, M. Ferrer, M. Townsend, A. L. Wolfe, M. A.
850 Seager, G. G. Kinney, P. J. Shughrue, W. J. Ray. Inhibition of calcineurin-mediated endocytosis and alpha-amino3-
851 hydroxy-5-methyl-4-isoxazolepropionic acid (AMPA) receptors prevents amyloid beta oligomer-induced synaptic
852 disruption. *J Biol Chem* **285**, 7619-7632 (2010).
853 51. N. R. Reinders, Y. Pao, M. C. Renner, C. M. da Silva-Matos, T. R. Lodder, R. Malinow, H. W. Kessels. Amyloidbeta
854 effects on synapses and memory require AMPA receptor subunit GluA3. *Proc Natl Acad Sci U S A* **113**, E6526E6534
855 (2016).
856 52. M. D. Ikonomovic, R. Sheffield, D. M. Armstrong. AMPA-selective glutamate receptor subtype immunoreactivity
857 in the hippocampal formation of patients with Alzheimer's disease. *Hippocampus* **5**, 469-486 (1995).
858 53. T. L. Carter, R. A. Rissman, A. J. Mishizen-Eberz, B. B. Wolfe, R. L. Hamilton, S. Gandy, D. M. Armstrong.
859 Differential preservation of AMPA receptor subunits in the hippocampi of Alzheimer's disease patients according
860 to Braak stage. *Exp Neurol* **187**, 299-309 (2004).
861 54. J. H. Y. Yeung, J. L. Walby, T. H. Palpagama, C. Turner, H. J. Waldvogel, R. L. M. Faull, A. Kwakowsky.
862 Glutamatergic receptor expression changes in the Alzheimer's disease hippocampus and entorhinal cortex. *Brain*
863 *Pathol* **31**, e13005 (2021).
864 55. B. G. Jang, S. In, B. Choi, M. J. Kim. Beta-amyloid oligomers induce early loss of presynaptic proteins in primary
865 neurons by caspase-dependent and proteasome-dependent mechanisms. *Neuroreport* **25**, 1281-1288 (2014).
866 56. M. C. Herzig, D. T. Winkler, P. Burgermeister, M. Pfeifer, E. Kohler, S. D. Schmidt, S. Danner, D. Abramowski, C.
867 Sturchler-Pierrat, K. Burki, S. G. van Duinen, M. L. Maat-Schieman, M. Staufenbiel, P. M. Mathews, M. Jucker.
868 Abeta is targeted to the vasculature in a mouse model of hereditary cerebral hemorrhage with amyloidosis. *Nat*
869 *Neurosci* **7**, 954-960 (2004).
870 57. L. Grand Moursel, W. M. C. van Roon-Mom, S. M. Kiełbasa, H. Mei, H. P. J. Buermans, L. M. van der Graaf, K.
871 M. Hettne, E. J. de Meijer, S. G. van Duinen, J. F. J. Laros, M. A. van Buchem, P. A. C. t Hoen, S. M. van der
872 Maarel, L. van der Weerd. Brain Transcriptomic Analysis of Hereditary Cerebral Hemorrhage With Amyloidosis
873 Dutch Type. *Front Aging Neurosci* **10**, 102 (2018).
874 58. R. A. Neff, M. Wang, S. Vatansever, L. Guo, C. Ming, Q. Wang, E. Wang, E. Horgusluoglu-Moloch, W.-m. Song,
875 A. Li, E. L. Castranio, J. Tcw, L. Ho, A. Goate, V. Fossati, S. Noggle, S. Gandy, M. E. Ehrlich, P. Katsel, E. Schadt,
876 D. Cai, K. J. Brennand, V. Haroutunian, B. Zhang. Molecular subtyping of Alzheimer's disease using RNA
877 sequencing data reveals novel mechanisms and targets. *Science Advances* **7**, eabb5398 (2021).
878 59. A. Jishi, X. Qi, H. C. Miranda. Implications of mRNA translation dysregulation for neurological disorders. *Semin*
879 *Cell Dev Biol* **114**, 11-19 (2021).
880 60. A. Ghosh, K. Mizuno, S. S. Tiwari, P. Proitsi, B. Gomez Perez-Nievas, E. Glennon, R. T. Martinez-Nunez, K. P.
881 Giese. Alzheimer's disease-related dysregulation of mRNA translation causes key pathological features with ageing.
882 *Translational Psychiatry* **10**, 192 (2020).

61. G. Joshi, Y. Chi, Z. Huang, Y. Wang. Aβ-induced Golgi fragmentation in Alzheimer's disease enhances Aβ production. *Proc Natl Acad Sci U S A* **111**, E1230-1239 (2014).
62. M. Calvo-Rodriguez, S. S. Hou, A. C. Snyder, E. K. Kharitonova, A. N. Russ, S. Das, Z. Fan, A. Muzikansky, M. Garcia-Alloza, A. Serrano-Pozo, E. Hudry, B. J. Bacskai. Increased mitochondrial calcium levels associated with neuronal death in a mouse model of Alzheimer's disease. *Nat Commun* **11**, 2146 (2020).
63. A.V. Venkataraman, A. Mansur, G. Rizzo, C. Bishop, Y. Lewis, E. Kocagoncu, A. Lingford-Hughes, M. Huiban, J. Passchier, J.B. Rowe, H. Tsukada, D. J. Brooks, L. Martarello, R. A. Comley, L. Chen, A.J. Schwarz, R. Hargreaves, R.N. Gunn, E. A. Rabiner, P. M. Matthew. Widespread cell stress and mitochondrial dysfunction occur in patients with early Alzheimer's disease. *Sci Transl Med.* **14**(658), eabk1051. doi: 10.1126/scitranslmed.abk1051. (2022).
64. M. Balietti, B. Giorgetti, T. Casoli, M. Solazzi, F. Tamagnini, C. Burattini, G. Aicardi, P. Fattoretti. Early selective vulnerability of synapses and synaptic mitochondria in the hippocampal CA1 region of the Tg2576 mouse model of Alzheimer's disease. *J Alzheimers Dis* **34**, 887-896 (2013).
65. X. Wang, B. Su, H. G. Lee, X. Li, G. Perry, M. A. Smith, X. Zhu. Impaired balance of mitochondrial fission and fusion in Alzheimer's disease. *J Neurosci* **29**, 9090-9103 (2009).
66. C. D. Sanmartin, T. Adasme, C. Hidalgo, A. C. Paula-Lima. The antioxidant N-acetylcysteine prevents the mitochondrial fragmentation induced by soluble amyloid-beta peptide oligomers. *Neurodegener Dis* **10**, 34-37 (2012).
67. T. Umeda, T. Tomiyama, N. Sakama, S. Tanaka, M. P. Lambert, W. L. Klein, H. Mori. Intraneuronal amyloid beta oligomers cause cell death via endoplasmic reticulum stress, endosomal/lysosomal leakage, and mitochondrial dysfunction in vivo. *J Neurosci Res* **89**, 1031-1042 (2011).
68. T. Umeda, E. M. Ramser, M. Yamashita, K. Nakajima, H. Mori, M. A. Silverman, T. Tomiyama. Intracellular amyloid β oligomers impair organelle transport and induce dendritic spine loss in primary neurons. *Acta Neuropathol Commun* **3**, 51 (2015).
69. L. Hedskog, C. M. Pinho, R. Filadi, A. Rönnbäck, L. Hertwig, B. Wiehager, P. Larssen, S. Gellhaar, A. Sandebring, M. Westerlund, C. Graff, B. Winblad, D. Galter, H. Behbahani, P. Pizzo, E. Glaser, M. Ankarcrona. Modulation of the endoplasmic reticulum–mitochondria interface in Alzheimer's disease and related models. *Proceedings of the National Academy of Sciences* **110**, 7916-7921 (2013).
70. C. H. van Dyck, C. J. Swanson, P. Aisen, R. J. Bateman, C. Chen, M. Gee, M. Kanekiyo, D. Li, L. Reyderman, S. Cohen, L. Froelich, S. Katayama, M. Sabbagh, B. Vellas, D. Watson, S. Dhadda, M. Irizarry, L. D. Kramer, T. Iwatsubo. Lecanemab in Early Alzheimer's Disease. *New England Journal of Medicine*, (2022).
71. J.R. Sims, J.A. Zimmer, C.D. Evans, M. Lu, P. Ardayfio, J. Sparks, A.M. Wessels, S. Shcherbinin, H. Wang, E.S. Monkul Nery, E.C. Collins, P. Solomon, S. Salloway, L.G. Apostolova, O. Hansson, C. Ritchie, D.A. Brooks, M. Mintun, D.M. Skoyronsky; TRAILBLAZER-AL2 Investigators. Donanemab in Early Symptomatic Alzherimer Disease: The TRAILBLAZER-ALZ 2 Randomized Clinical Trial. *JAMA.* **330**, 512-527. Doi: 10.001/jama.2023.13239 (2023).
72. H. Sun, Y. Wang, Y. Wang, F. Zeng. Case of Autosomal Dominant Alzheimer Disease With Negative Findings From PiB-PET Examination. *Neurol Genet* **10**, e200119 (2024).
73. C. A. Schneider, W. S. Rasband, K. W. Eliceiri. NIH Image to ImageJ: 25 years of image analysis. *Nat Methods* **9**, 671-675 (2012).
74. M. Pagnon de la Vega, V. Giedraitis, W. Michno, L. Kilander, G. Güner, M. Zielinski, M. Löwenmark, R. Brundin, T. Danfors, L. Söderberg, I. Alafuzoff, L. N. G. Nilsson, A. Erlandsson, D. Willbold, S. A. Müller, G. F. Schröder, J. Hanrieder, S. F. Lichtenthaler, L. Lannfelt, D. Sehlin, M. Ingelsson. The Uppsala APP deletion causes early onset autosomal dominant Alzheimer's disease by altering APP processing and increasing amyloid β fibril formation. *Sci Transl Med* **13**, (2021).
75. S. R. Meier, D. Sehlin, G. Hultqvist, S. Syvänen. Pinpointing Brain TREM2 Levels in Two Mouse Models of Alzheimer's Disease. *Mol Imaging Biol* **23**, 665-675 (2021).
76. J. W. Steele, H. Brautigam, J. A. Short, A. Sowa, M. Shi, A. Yadav, C. M. Weaver, D. Westaway, P. E. Fraser, P. H. St George-Hyslop, S. Gandy, P. R. Hof, D. L. Dickstein. Early fear memory defects are associated with altered synaptic plasticity and molecular architecture in the TgCRND8 Alzheimer's disease mouse model. *J Comp Neurol* **522**, 2319-2335 (2014).

933 77. M. J. Lazarczyk, J. E. Kemmler, B. A. Eyford, J. A. Short, M. Varghese, A. Sowa, D. R. Dickstein, F. J. Yuk, R.
934 Puri, K. E. Biron, M. Leist, W. A. Jefferies, D. L. Dickstein. Major Histocompatibility Complex class I proteins are
935 critical for maintaining neuronal structural complexity in the aging brain. *Sci Rep* **6**, 26199 (2016).
936 78. Y. Hara, M. Punsoni, F. Yuk, C. S. Park, W. G. Janssen, P. R. Rapp, J. H. Morrison. Synaptic distributions of GluA2
937 and PKMzeta in the monkey dentate gyrus and their relationships with aging and memory. *J Neurosci* **32**, 73367344
938 (2012).
939 79. Y. Hara, C. S. Park, W. G. Janssen, M. T. Roberts, J. H. Morrison, P. R. Rapp. Synaptic correlates of memory and
940 menopause in the hippocampal dentate gyrus in rhesus monkeys. *Neurobiol Aging* **33**, 421 e417-428 (2012).
941 80. Y. Han, P. S. Kaeser, T. C. Südhof, R. Schneggenburger. RIM determines Ca^{2+} channel density and vesicle docking
942 at the presynaptic active zone. *Neuron* **69**, 304-316 (2011).
943 81. C. Tan, S. S. H. Wang, G. de Nola, P. S. Kaeser. Rebuilding essential active zone functions within a synapse. *Neuron*
944 **110**, 1498-1515.e1498 (2022).
945 82. P. G. Camoletto, H. Vara, L. Morando, E. Connell, F. P. Marletto, M. Giustetto, M. Sassoè-Pognetto, P. P. Van
946 Veldhoven, M. D. Ledesma. Synaptic vesicle docking: sphingosine regulates syntaxin1 interaction with Munc18.
947 *PLoS One* **4**, e5310 (2009).
948 83. A. Butler, P. Hoffman, P. Smibert, E. Papalexi, R. Satija. Integrating single-cell transcriptomic data across different
949 conditions, technologies, and species. *Nature Biotechnology* **36**, 411 (2018).
950 84. L. McInnes, J. Healy, J. Melville. UMAP: Uniform Manifold Approximation and Projection for Dimension
951 Reduction. *arXiv* **1802.03426**, (2018).
952 85. O. Franzén, L.-M. Gan, J. L. M. Björkegren. PanglaoDB: a web server for exploration of mouse and human
953 singlecell RNA sequencing data. *Database* **2019**, (2019).
954 86. A. Butler, P. Hoffman, P. Smibert, E. Papalexi, R. Satija. Integrating single-cell transcriptomic data across different
955 conditions, technologies, and species. *Nature biotechnology* **36**, 411-420 (2018).
956 87. R. Satija, J. A. Farrell, D. Gennert, A. F. Schier, A. Regev. Spatial reconstruction of single-cell gene expression data.
957 *Nat Biotechnol* **33**, 495-502 (2015).
958 88. C. Neftel, J. Laffy, M. G. Filbin, T. Hara, M. E. Shore, G. J. Rahme, A. R. Richman, D. Silverbush, M. L. Shaw,
959 C. M. Hebert, J. Dewitt, S. Gritsch, E. M. Perez, L. N. Gonzalez Castro, X. Lan, N. Druck, C. Rodman, D. Dionne,
960 A. Kaplan, M. S. Bertalan, J. Small, K. Pelton, S. Becker, D. Bonal, Q. D. Nguyen, R. L. Servis, J. M. Fung, R.
961 Mylvaganam, L. Mayr, J. Gojo, C. Haberler, R. Geyeregger, T. Czech, I. Slavc, B. V. Nahed, W. T. Curry, B. S.
962 Carter, H. Wakimoto, P. K. Brastianos, T. T. Batchelor, A. Stemmer-Rachamimov, M. Martinez-Lage, M. P. Frosch,
963 I. Stamenkovic, N. Riggi, E. Rheinbay, M. Monje, O. Rozenblatt-Rosen, D. P. Cahill, A. P. Patel, T. Hunter, I. M.
964 Verma, K. L. Ligon, D. N. Louis, A. Regev, B. E. Bernstein, I. Tirosh, M. L. Suva. An Integrative Model of Cellular
965 States, Plasticity, and Genetics for Glioblastoma. *Cell* **178**, 835-849 e821 (2019).
966 89. Y. Hara, F. Yuk, R. Puri, W. G. Janssen, P. R. Rapp, J. H. Morrison. Presynaptic mitochondrial morphology in
967 monkey prefrontal cortex correlates with working memory and is improved with estrogen treatment. *Proc Natl Acad*
968 *Sci U S A* **111**, 486-491 (2014).
969 90. Y. He, P. R. Hof, W. G. M. Janssen, J. D. Rothstein, J. H. Morrison. Differential synaptic localization of GluR2 and
970 EAAC1 in the macaque monkey entorhinal cortex: a postembedding immunogold study. *Neuroscience Letters* **311**,
971 161-164 (2001).
972 91. Y. Zhou, B. Zhou, L. Pache, M. Chang, A. H. Khodabakhshi, O. Tanaseichuk, C. Benner, S. K. Chanda. Metascape
973 provides a biologist-oriented resource for the analysis of systems-level datasets. *Nat Commun* **10**, 1523 (2019).
974 92. K. D. Micheva, N. O'Rourke, B. Busse, S. J. Smith. Array tomography: high-resolution three-dimensional
975 immunofluorescence. *Cold Spring Harb Protoc* **2010**, pdb top89 (2010).
976 93. K. D. Micheva, N. O'Rourke, B. Busse, S. J. Smith. Array tomography: imaging-stained arrays. *Cold Spring Harb*
977 *Protoc* **2010**, pdb prot5526 (2010).
978 94. J. Schindelin, I. Arganda-Carreras, E. Frise, V. Kaynig, M. Longair, T. Pietzsch, S. Preibisch, C. Rueden, S. Saalfeld,
979 B. Schmid, J.-Y. Tinevez, D. J. White, V. Hartenstein, K. Eliceiri, P. Tomancak, A. Cardona. Fiji: an open-source
980 platform for biological-image analysis. *Nature Methods* **9**, 676-682 (2012).
981 95. K. R. Kay, C. Smith, A. K. Wright, A. Serrano-Pozo, A. M. Pooler, R. Koffie, M. E. Bastin, T. H. Bak, S. Abrahams,
982 K. J. Kopeikina, D. McGuone, M. P. Frosch, T. H. Gillingwater, B. T. Hyman, T. L. Spires-Jones. Studying synapses
983 in human brain with array tomography and electron microscopy. *Nat Protoc* **8**, 1366-1380 (2013).

96. A. Cardona, S. Saalfeld, J. Schindelin, I. Arganda-Carreras, S. Preibisch, M. Longair, P. Tomancak, V. Hartenstein, R. J. Douglas. TrakEM2 software for neural circuit reconstruction. *PLoS One* **7**, e38011 (2012).
97. R. Kayed, E. Head, J. L. Thompson, T. M. McIntire, S. C. Milton, C. W. Cotman, C. G. Glabe, Common structure of soluble amyloid oligomers implies common mechanism of pathogenesis. *Science* **300**, 486-489 (2003).
98. R. Kayed, E. Head, F. Sarsoza, T. Saing, C.W. Cotman, M. Necula, L. Margol, J. Wu, L. Breydo, J.L. Thompson, S. Rasool, T. Gurlo, P. Butler, C.G. Glabe. Fibril specific, conformation dependent antibodies recognize a generic epitope common to amyloid fibrils and fibrillar oligomers that is absent in prefibrillar oligomers. *Mol Neurodegener.* **2**, 18. doi: 10.1186/1750-1326-2-18 (2007).
99. M. Richman, S. Wilk, M. Chemerovski, S.K. Wärmländer, A. Wahlström, A. Gräslund, S. Rahimipour. *In vitro* and mechanistic studies of an antiamyloidogenic self- assembled cyclic D, L-α-peptide architecture. *J Am Chem Soc.* **135**, 3474-84 (2016).
100. M. Chemerovski-Glikman, M. Richman, S. Rahimipour. Structure-based study of antiamyloidogenic cyclic D,L-α-peptides. *Tetrahedron* **70**, 7639–7644 (2014).
101. M. Chemerovski-Glikman, E. Rozentur-Shkop, M. Richman, A. Grupi, A. Getler, H. Y. Cohen, H. Shaked, C. Wallin, S. K. Wärmländer, E. Haas, A. Gräslund, J. H. Chill, S. Rahimipour. Self-assembled cyclic D,L-alpha-peptides as generic conformational inhibitors of the alpha-synuclein aggregation and toxicity: In vitro and mechanistic studies. *Chemistry*, ***22***, 14236-14246 (2016).
102. A. Belostozky, M. Richman, E. Lisniansky, A. Tovchygrechko , J. Chill, S. Rahimipour. Inhibition of tau-derived hexapeptide aggregation and toxicity by a self-assembled cyclic d,l-α-peptide conformational inhibitor. *Chem Commun (Camb).* **54**, 5980-5983. doi: 10.1039/c8cc01233d (2018).
103. K. Ono, M.M. Condron, D. B. Teplow. Structure-neurotoxicity relationships of amyloid beta-protein oligomers. *Proc. Natl. Acad. Sci. U. S. A.* **106,** 14745-14750 (2009).
104. R.J. Rodenburg. Biochemical diagnosis of mitochondrial disorders. *J Inherit Metab Dis* **34**,283-92 (2011).
105. T.L. Emmerzaal, R.J. Rodenburg, H. Tanila, V. Verweij, A.J. Kiliaan, T. Kozicz T. Age-Dependent Decrease of Mitochondrial Complex II Activity in a Familial Mouse Model for Alzheimer's Disease. *J Alzheimers Dis.* **66**, 75-82. doi: 10.3233/JAD-180337 (2018).
106. M. Noguchi-Shinohara, K. Shuta, H. Murakami, Y. Mori, J. Komatsu, C. Kobayashi, S. Hersch, K. Horie, K. Ono. Lecanemab-Associated Amyloid-β Protofibril in Cerebrospinal Fluid Correlates with Biomarkers of Neurodegeneration in Alzheimer's Disease. *Ann Neurol.* doi: 10.1002/ana.27175. (2025).
107. D. Shea, E. Colasurdo, A. Smith, C. Paschall, S. Jayadev, C.D. Keene, D. Galasko, A. Ko, G. Li, E. Peskind, V. SOBA: Development and testing of a soluble oligomer binding assay for detection of amyloidogenic toxic oligomers. *Proc Natl Acad Sci U S A.* **119**: e2213157119. doi: 10.1073/pnas.2213157119 (2022).
108. Choi, E.H., Kim, M.H., Park, S.J. Targeting mitochondrial dysfunction and reactive oxygen species for neurodegenerative disease treatment. *International journal of molecular sciences*, 25(14), p.7952. 109 (2024).
109. Xu, J., Du, W., Zhao, Y., Lim, K., Lu, L., Zhang, C., Li, L. Mitochondria targeting drugs for neurodegenerative diseases—Design, mechanism and application. *Acta Pharmaceutica Sinica B*, 12(6), pp.2778-2789, (2022).
110. E. Andersson, N. Lindblom, S. Janelidze, G. Salvadó, E. Gkanatsiou, L. Söderberg, C. Möller, L. Lannfelt, J. Ge, J. Hanrieder, K. Blennow, T. Deierborg, N. Mattsson-Carlgren, H. Zetterberg, G. Gouras, O. Hansson. Soluble cerebral Aβ protofibrils link Aβ plaque pathology to changes in CSF $A\beta_{42}/A\beta_{40}$ ratios, neurofilament light and tau in Alzheimer's disease model mice. *Nat Aging*. doi: 10.1038/s43587-025-00810-8. (2025).

Acknowledgments

We would like to thank all the members of the Dickstein, Arancio, Levy, Rahimipour, Lubell, Guerin, and Ehrlich/Gandy laboratories, and William G. M. Janssen, Allison Sowa, Daniel R. Dickstein, Frank Yuk, and Michael Ragusa for technical assistance and discussion. The authors would like to thank Yanzhuang Wang (Shenzhen Bay Laboratory), and Gary Gibson, Giovanni Manfredi, and Csaba Konrad (all from Weill Cornell Medical College) for valuable conversations and suggestions. We also thank Tamas Kozicz and Graeme Preston (Icahn School of Medicine at Mount Sinai) for performing the electron transport chain activity assays.

Funding:

National Institutes of Health grant F32AG077900 (ELC)
National Institutes of Health grant P30 AG066514 to Mary Sano with Developmental Pilot Award (ELC, SG)
National Institutes of Health grant U01AG046170 (SG, MEE, MW, BZ)
National Institutes of Health grant RF1AG058469 (SG, MEE)
National Institutes of Health grant RF1AG059319 (SG, MEE)
National Institutes of Health grant R01AG061894 (SG, MEE)
Cure Alzheimer's Fund (SG, MEE, SR, BG, WL)
National Institutes of Health grant RF1AG057440 (MW, BZ)
National Institutes of Health grant R56AG056507 (CG)
National Institutes of Health grant AG056732 (EL)
National Institutes of Health grant R01NS110024 (OA)
Alzheimer's Association NIRG-12-242386 (DLD)
Medical Student Training in Aging Research Program Scientific Fellowship from the American Federation for Aging Research (EB)
The Linda Wachner Foundation (SG, MEE)
National Institutes of Health grant RF1AG077828 (MW)
National Institutes of Health grant R21AG077168 (MW)
Alzheimer's Association AARG-22-928419 (MW)

Author contributions:

Conceptualization: MEE, SG, EL, DLD, OA
Methodology: EB, MV, DLD, KT, SH, JVDL, OA, EA, ELC, CDS, MW, BZ, CG, SR
Investigation: RT, MV, DL, EB, DLD, FG, ELC, KT, SH, JVDL, OA, EA, HZ, BZ, MW, CDS, LS, LL, MI, SR
Visualization: MV, DLD, KT, SH, ELC, MW
Supervision: MEE, SG, EL, DLD, OA
Writing—original draft: MV, DLD, EB, ELC, SG, EA, OA, MW
Writing—review & editing: MV, DLD, ELC, SG, MEE, EL, CG, SR, WL, BG

Competing interests: Dr. Gandy is a co-founder of Recuerdo Pharmaceuticals. He has served as a consultant in the past for J&J, Diagenic, and Pfizer, and he currently consults for Cognito Therapeutics, GLG Group, SVB Securities, Guidepoint, Third Bridge, MEDACORP, Altpep, Vigil Neurosciences, Memory Garden, and Eisai. He has received research support in the past from Warner-Lambert, Pfizer, Baxter, and Avid. The authors declare no other competing interests.

Data and materials availability: The scRNA-seq data (cell ranger processed count matrices) are in a Synapse repository (accession syn52752404, with direct link https://www.synapse.org/#!Synapse:syn52752404/files/). All data are available in the main text or the supplementary materials." The APP^{E693Q} transgenic mouse can be provided by Thomas Jefferson University pending scientific review and a completed material transfer agreement. Requests for the APP^{E693Q} transgenic mouse should be submitted to michelle.ehrlich@mssm.edu.

Disclaimer

The opinions expressed herein are those of the authors and are not necessarily representative of those of the government of the United States, the Uniformed Services University of the Health Sciences, the Department of Defense (DoD), or the United States Army, Navy or Air Force or the Henry M. Jackson Foundation for the Advancement of Military Medicine, Inc.

Supplementary Materials Table of Contents

Supplementary Methods
Figs. S1 to S15
References (92 to 110)

1076 **Figure Captions**

1077 **Figure 1. Aging-related accumulation of NFA-Aβ in the cerebral cortex of APP^{E693Q} transgenic mice**
1078 **revealed by double labeling with A11 epitomic immunohistochemistry and CP-2 cyclic peptide-FITC**
1079 **fluorescence microscopy.** Representative images from 24-month-old Dutch mice showing fluorescence
1080 microscopy using DAPI, A11 staining with AlexaFluor-680 secondary antibody (red), and CP-2 cyclic
1081 peptideFITC (CP-2-FITC, green)(*22*). Lower right panel is a merge of A11 and CP-2-FITC images. Scale bar =
1082 100 µm. Quantification of A11-immunoreactive and CP-2-FITC-immunoreactive NFA-Aβ aggregates in 2- and
1083 24mo Dutch shown in Figure S1C. ** $p < 0.01$.

1084

1085 **Figure 2. Dutch mice do not exhibit impairment in basal synaptic transmission or LTP. (A, B)** Basal
1086 neurotransmission **(A)** and LTP **(B)** are unimpaired in hippocampal slices from Dutch mice as compared to
1087 slices from wildtype littermates at the age of 7 to 7.5 months ($F_{(1,28)}$ =0.0026, p=0.959 and $F_{(1,28)}$ =0.219,
1088 p=0.644, respectively). **(C-D)** Slices from Dutch mice do not exhibit impairment of basal neurotransmission **(C)**
1089 and LTP **(D)** at the age of 10.5 to 11 months compared to wildtype mice ($F_{(1,18)}$ =0.116, p=0.737 and $F_{(1,18)}$
1090 =0.017, =0.899, respectively).

1091

1092 **Figure 3. Distribution and ultrastructure of mGluR-2/3-labeled synapses were comparable in the CA1 of**
1093 **12-monthold Dutch and wildtype mice.** mGluR-2/3-labeled synapses were defined as having ≥1 immunogold
1094 particle located in the PSD or synaptic cleft. **(A-C)** No significant differences were observed between Dutch and
1095 wildtype mice in percentage of mGluR-2/3-labeled total, perforated, and non-perforated synapses, respectively.
1096 **(D-F)** Average PSD area of mGluR-2/3labeled synapses for all synapses, non-perforated synapses, and perforated
1097 synapses, respectively. Dutch mice had larger PSD area of mGluR-2/3-labeled non-perforated synapses than
1098 wildtype (p= 0.04, by unpaired t test), whereas perforated synapses or total synapses were comparable between
1099 the two groups. **(G-I)** No significant difference was observed in density of immuno-gold particles in mGluR-2/3-
1100 labeled synapses, calculated as number of immuno-gold particles/ PSD area, for all synapses, non-perforated
1101 synapses, and perforated synapses, respectively. Data are mean ± SD from n = 5 wildtype, and n = 4 Dutch mice.

1102

1103 **Figure 4. Dutch mice showed impairment of certain measurements of short-term synaptic plasticity.**
1104 **(A)** Dutch mice showed no impairment in paired-pulse facilitation at the age of 11 to 13 months old ($F_{(1, 220)}$
1105 =0.06364, p=0.8011; 2-way ANOVA). **(B)** Post-tetanic potentiation was significantly reduced in slices from 11-
1106 to 13-month-old Dutch mice compared to wildtype ($F_{(1,36)}$ =4.771, p=0.036; 2-way ANOVA for the first 6 points
1107 after potentiation). **(C)** Significant differences were observed in synaptic fatigue when comparing slices from
1108 Dutch mice and wildtype littermates (k=2.247±0.1622 for wildtype and k=2.782±0.1634 for Dutch, p=0.015, k:

109 rate of exponential decay). **(D)** The rate of synaptic vesicle replenishment following a 100 Hz stimulation was
110 found to be significantly increased in hippocampal slices from Dutch mice as compared to slices from wildtype
111 littermates (k=7.509±0.7277 for wildtype, k=13.64±1.682 for Dutch, p<0.0001, k: rate of exponential growth).
112
113 **Figure 5. Synaptic distribution of mGluR-2/3 in the CA1 is comparable in 12-month-old wildtype and**
114 **Dutch mice. (A-C)** Examples of mGluR-2/3 immuno-gold staining. Note the distribution of immuno-gold
115 particles within the presynaptic terminal (purple masks) and the postsynaptic dendritic spine (cyan masks). Scale
116 bars = 500 nm. **(D)** Schematic diagram demonstrating the 6 synaptic bins used to categorize the localization of
117 each gold particle (adapted from (*90*)). Bin A, active zone (presynaptic, within 45 nm of the membrane across
118 from the PSD); B, synaptic cleft; C, postsynaptic density (PSD); D, peri-synaptic (Peri-PSD, on the postsynaptic
119 spine head, within 200 nm of the PSD); E, postsynaptic membrane (>200 nm away from the PSD) and F,
120 postsynaptic cytoplasm (cytosol). **(E)** Distribution of immuno-gold labeled mGluR-2/3 among the various regions
121 of the synapse showed no significant differences between wildtype and Dutch mice. Data are mean ± SD from
122 wildtype (n = 5) and Dutch (n = 4) (repeated measures ANOVA).
123
124 **Figure 6. Transcriptional responses in Dutch mouse brains. (A)** scRNA-seq of hippocampal tissues from 12-
125 month-old male and female Dutch and wildtype mice (n=2 samples per sex per genotype with 3 mice pooled per
126 sample). UMAP plot showing 14 distinguishable clusters (0-13). **(B)** Violin plots illustrating expression of marker
127 genes for each cell type. **(C)** UpSet plot highlighting the overlapping and unique genes between the clusters. **(D)**
128 Bar plot showing number of DEGs per cluster by directionality.
129
130 **Figure 7. Overlapping transcriptomic profiles highlight processes impacted in multiple cell types. (A)** Dot
131 plot highlighting shared GO term enrichment across clusters. **(B-C)** Dot plot of genes associated with shared
132 GO terms **(B)** "structural constituent of ribosome" and **(C)** "amyloid-beta binding", split into Dutch and
133 wildtype mice across all clusters. Wildtype mice are in blue, Dutch mice are in purple. **(D)** UpSet plot
134 comparing overlap of cluster DEGs (adj. p-value <0.05) with previously defined aging gene list. **(E)** Heatmap of
135 log2FC of genes shared with aging gene list.
136
137 **Figure 8. Microglia transcriptomic profiles are similar between Dutch and wildtype mice. (A)** UMAP plot
138 showing sub-clustering analysis results for Cluster 2 microglia, identifying 3 subpopulations of microglia with
139 UMAP plot split by genotype to the right. **(B)** UMAP plots showing expression of previously identified microglial
140 signatures; DAM(*33*), homeostatic, IFN and MHC(*34*). **(C)** Violin plots showing expression across subclusters
141 by genotypes of selected homeostatic microglial genes.

Figure 9. Transcriptional profile of Cluster 6 excitatory neurons is altered in Dutch mice. (A) Volcano plot of genes enriched in Cluster 6 as calculated by pseudobulk differential expression analysis. Red genes are Log2FC > 0.25 and adj. p-value < 0.05, blue Log2FC < 0.25 and adj. p-value < 0.05, green genes are Log2FC > 0.25 and adj. p-value > 0.05, and grey genes are Log2FC < 0.25 and adj. p-value > 0.05. **(B-C)** GO term analysis of **(B)** upregulated and **(C)** downregulated genes enriched in Cluster 6 (adj. p-value < 0.05) using metascape(*91*). **(D)** Dot plot of DEGs unique to Cluster 6.

Figure 10. Fewer mitochondria were present in presynaptic boutons at excitatory synapses in the CA1 of 12-month-old Dutch mice compared to wildtype. **(A)** Electron micrographs showing representative examples of presynaptic mitochondria (blue masks). **(B)** Curved presynaptic mitochondria demonstrate a bend of at least 90°. Straight presynaptic mitochondria did not exhibit any curvature. Scale bar = 500 nm. **(C)** Total number, **(D)** number of straight mitochondria, **(E)** number of curved mitochondria, **(F)** percentage of curved mitochondria, **(G)** average diameter, and **(H)** number of layers traversed by each mitochondrion in wildtype and Dutch mice. Data are mean ± SD from n = 4 wildtype and n = 5 Dutch mice.

158 **Supplementary Tables Titles and Captions**

159 **Supplementary Table 1. Cluster Cell Numbers.** Number of cells per cluster per sample.

160 **Supplementary Table 2. Cluster Markers.** De novo cluster signatures calculated by comparing cell clusters
161 using Wilcox rank sum test in Seurat.

162 **Supplementary Table 3. Cluster DEGs.** Differentially expressed genes across all 14 clusters using MAST
163 implemented in Seurat.

164 **Supplementary Table 4. Cluster 6 GO-terms.** GO-term analysis of genes enriched in Cluster 6 (l2f>0, padj
165 <0.05) using metascape.

166 **Supplementary Table 5. Cluster 6 GO-terms.** GO-term analysis of genes enriched in Cluster 6 (l2f<0, padj
167 <0.05) using metascape.

168 **Supplementary Table 6. Cluster 4 GO-terms.** GO-term analysis of genes enriched in Cluster 6 (l2f>0, padj
169 <0.05) using metascape.

170 **Supplementary Table 7. Ligand-Receptor Pairs for Clusters 6 and 4.** Cell-cell communication analysis
171 calculated by Cellphone DB to compute interaction between Clusters 6 and Clusters 9 based on known Ligand-
172 Receptor pairs. t-test was used to compare interaction strength differences between Dutch and WT mice

173 **Supplementary Table 8. Mitochondrial electron transport chain (mETC) enzymology. mETC complexes**
174 **standardized to μg protein.**

175 **Supplementary Table 9. Mitochondrial electron transport chain (mETC) enzymology. mETC complexes**
176 **standardized to mU/ml citrate synthase.**

177

178

Supplementary Materials for

Endogenously generated Dutch-type Aβ nonfibrillar aggregates dysregulate presynaptic neurotransmission in the absence of detectable inflammation.

Emilie L. Castranio *et al.*

*Corresponding author. Email: michelle.ehrlich@mssm.edu

This PDF file includes:

Supplementary Methods
Figs. S1 to S15
References (92 to 110)

Supplemental Text, Methods, and Data

Cyclic peptide interactions with Aβ oligomers (NFA-Aβ)

The concept that NFA-Aβ of various polypeptide sequences might share structural features was first introduced by Kayed *et al.* (2007) (*97,98*) who showed that oligomers of Aβ, IAPP, lysozyme, α-synuclein, prion protein, insulin, and polyglutamine are equally recognized by antibodies that were generated against Aβ oligomers and fibrils. A11 and OC are two antibodies that can each detect unique oligomer subtypes by binding to generic higher order structural epitopes (*97,98*). Richman *et al.* (2013) (*99*) screened a library of six-residue cyclic D,L-α-peptides and identified short peptides that could accomplish a similar goal. Cyclic D,L-α-peptides comprised of even numbers of alternating D- and L-α-amino acids self-assemble into nanotube structures that replicate the intermolecular hydrogen-bonding patterns of cross β-sheets with features of amyloid proteins such as interstrand distances of 4.8 Å (*99*). At and above stoichiometric concentrations, cyclic peptide CP-2 (*c*-[Lys^1-D-Leu^2-Nle^3-D-Trp^4-His^5-D-Ser^6]) was shown to engage soluble and low molecular weight Aβ species, modulate aggregation, disassemble fibrils, and inhibit cell toxicity by an "off-pathway" mechanism (*99, 100*). CP-2 also bound other aggregation-prone polypeptides including PD-associated α-synuclein (α-syn) and tau-derived hexapeptide AcPHF6 (*101, 102*). Various biochemical methods have been employed to demonstrate either the binding of CPs to oligomers or the catalytic effects of cyclic peptides on oligomer structure. These include photoinduced cross-linking of unmodified proteins (PICUP) combined with SDS/PAGE) (*99*) and dynamic light scattering (DLS) (*22*). In some experiments, an aza derivative of CP-2 (CP-7) was prepared, and DLS was used to determine its effect on the size of Aβ40 NFA-Aβ. According to different microscopy techniques including atomic force microscopy and electron microscopy, the size of the NFA-Aβ is around 10 nm (*103*).

Array tomography

Array tomography (AT) is a high-resolution imaging technique that permits immunofluorescence imaging of multiple targets with unprecedented resolution and quantitative reliability (*92*). To prepare samples for AT, sections from CA1 were blocked in ~2 mm x ~1 mm sections, embedded in the acrylic resin LR White, dehydrated in graded series of ethanol (30%, 40%, 50%, 70% for 10 minutes each at 4 °C) and then transferred to a mixture of 1:3 70% ethanol and LR White (Electron Microscopy Sciences, EMS #14384-UC) for 15 minutes at 4 °C. Subsequently, tissues were placed in 100% LR White for two cycles of 15 minutes at 4 °C and then transferred to fresh 100% LR White overnight. On the second day, the tissue was incubated in pure 100% LR White for two 2-hour intervals at 4°C. Each block of tissue was placed at the bottom of a flow-through capsule and inserted into a BEEM capsule (EMS #7000B) with a corresponding label. A master solution of 10 ml of LR White and one drop of LR White Accelerator (London Resin Company) was used to fill the BEEM capsules and left to

polymerize overnight in a water bath at 4°C. Embedded tissue samples were stored at room temperature until they were cut. A histology knife (DiATOME) was used to remove excess resin and to expose the tissue surface. Sample sections of 70 nm were stained with toluidine blue to confirm the region of interest and to plan trimming area. Next, an ultratrim 45° knife (DiATOME) was used to trim the block face to an area of 2 mm x 1 mm. A Coat-Quick G pen (EMS #70624) was used to apply a small layer of glue to the bottom of the block face to hold the serial sections together as they form a strip. Strips of 15-50 sequential, ultra-thin, 70 nm serial sections were cut using a Jumbo histology knife and mounted on Superfrost Plus charged slides.

Tissue strips were circled with Aqua Hold Pap Pen (EMS #71311) and rehydrated with glycine (50 nM in Tris buffered saline, TBS) for 5 minutes in a humid chamber. Following a rinse with blocking solution (94% TBS, 1% bovine serum albumin BSA, and 5% Tween 20) samples were incubated in additional blocking solution for 5 minutes. Anti-mGluR-2/3 antibody (1:100, Millipore, AB1506) was applied to serial strips and incubated at 4 °C overnight in a humidifying chamber.

The following day, the strips were rinsed with TBS for 4 x 5 minutes at room temperature. Secondary antibody Alexa Fluor 488 donkey anti-rabbit IgG (1:400, Life Technologies, A-21206) and NeuroTrace 640/660 deep-red fluorescent Nissl stain (1:400, N-21483 Life Technologies) were applied to serial strips for 30 minutes at room temperature. The serial sections were rinsed with TBS for 4 x 5 minutes followed by one rinse in distilled water, mounted with Vecta Shield (Vector Labs, H-1000), coverslipped (CSHP-No 1.5-24 × 60; Bioscience Tools), and imaged immediately.

Images were acquired as described (*93*). Briefly, serial sections were imaged on an AxioImager.M2 microscope (Zeiss), equipped with an ORCA-R2 C10600-10B digital camera (Hamamatsu), and the Zen 2012 Blue Edition version 1.1.1.0 (Zeiss) imaging software. Areas of interest were initially identified using a 5x, N.A. 0.16 Plan-Apochromat objective (Zeiss). Once the region comprising the pyramidal neurons of the CA1 region was located, the tissue was imaged at higher magnification with a 63x, 1.4NA Plan-Apochromat objective (Zeiss). The exposure was adjusted for both channels (488 and 640 nm) and a blood vessel or a large cell body that would be visible in the following section was chosen as a landmark. The image of the first section was taken, and the stage was repositioned and aligned to the same landmark in the next section. If needed, the focus and/or exposure were adjusted, and the second image was collected. This process was repeated for the entire length of the serial strip, collecting 7-40 images per slide. The original images collected were converted from .czi to .tif format for subsequent analysis.

The serial images acquired for each sample were processed for analysis with FIJI (ImageJ, U. S. National Institutes of Health, Bethesda, Maryland, USA) (*94*). First, stacks were generated for each channel per sample using the Bioformats Importer Plug-In. Next, the background was subtracted (rolling ball diameter 50 pixels), and the image stacks were normalized (pixel saturation 0.1%) to adjust for variation in fluorescence between sections (*95*). The processed image stacks were aligned using the MultiStackReg plug-in (courtesy of the Smith

laboratory, Stanford, CA). The NeuroTrace channel was aligned and used as a reference for subsequent alignments of mGluR-2/3. Stacks that could not be automatically aligned were aligned manually using TrakEM2 plug-in (*96*). To analyze the puncta, a threshold was set for each channel using FIJI. To exclude imaging artifacts and cell bodies, thresholds were adjusted so that only punctate signal for the synaptic protein channel remained. Then, images were processed through the Watershed program (Smith laboratory, Stanford, CA), which generates an output with the total number of puncta per image stack and the size, in voxels (3D pixels), of each punctum. These puncta data were used for statistical analysis.

Western blotting

Mouse brains were dissected, and the hippocampus was immediately snap-frozen and stored at -80 ˚C until processed. Tissue samples were suspended at 10% w/v in Tris-buffered saline (TBS), pH 7.6 with 1% v/v Triton X-100 with protease and phosphatase inhibitors (Halt protease inhibitor cocktail 1862209 and 1861274, Thermo Scientific, Rockford, IL and phosphatase inhibitor P5276, Sigma) and homogenized for 20 s at 5,000 rpm using a Precellys 24 homogenizer (Bertin Instruments, Montigny-le-Bretonneux, France). The homogenates were centrifuged at 1,200 x *g* for 10 minutes. Equal volumes of the supernatant were transferred to ultracentrifuge tubes, placed in a TLA-55 fixed-angle rotor, and centrifuged for 1 hour at 100,000xg at 4 °C using an Optima Max-XP tabletop ultracentrifuge (Beckman Coulter, Brea, CA). The supernatant was saved as the soluble fraction. The insoluble pellet was resuspended in 5 µl of TBS + 1% sodium dodecyl sulfate (SDS) with protease and phosphatase inhibitors for every mg of original tissue weight. This insoluble fraction was incubated for 20 minutes and centrifuged for 10 minutes at 16,000 x *g* using a 5254 R table-top centrifuge (Eppendorf, Hamburg, Germany). Protein concentrations were estimated with BCA protein assay (Pierce™ BCA Protein Assay Kit, Thermo Scientific). Samples were stored in -20 °C until ready for use. Samples were separated by electrophoresis on 12% Tris-Glycine SDS-polyacrylamide gels followed by transfer to PVDF membranes (Thermo Scientific, Rockford, IL). The membranes were then incubated in anti-glutamate receptor 2 & 3 (anti-mGluR-2/3, 0.2 µg/ml, rabbit polyclonal, AB1506, Millipore). The secondary antibody used was horseradish peroxidase (HRP)-conjugated goat anti-rabbit IgG (1:20,000, Santa Cruz Biotechnology sc-3837). Actin-HRP (1:1,000) was used to detect the housekeeping protein. Membranes were exposed to ECL (Western Lighting™ Plus-ECL, PerkinElmer) and imaged using ChemiDoc MP imaging system and Image Lab software (BioRad). When necessary, blots were stripped of primary antibody using low pH stripping buffer (25 mM glycine, pH 2.0 with 1% w/v SDS). Optical densities of bands were quantified using ImageJ software(*73*). Density was normalized to actin, and results are presented as percentages of wildtype average.

For the synaptic marker western blots, protein was extracted from hippocampi by homogenization in RIPA buffer (Thermo Fisher Scientific) containing phosphatase/protease inhibitor cocktail (Thermo Fisher Scientific) and centrifuged at 15,000 × *g* for 20 minutes at 4°C before collecting the supernatant. A 30 µg aliquot of total

protein was separated by electrophoresis in precast 4% to 12% Bis-Tris Gels (Bio-Rad) and transferred to nitrocellulose membranes. Membranes were blocked in 5% milk before probing with the following antibodies: mouse anti-PSD95 (clone 6G6-1C9, 1:4000, EMD Millipore, MAB1596), rabbit anti-synaptophysin (1:1000, Abcam, ab16659), and mouse anti-GAPDH (1:2000, SantaCruz, sc-32233). The secondary antibody used was peroxidase-labelled anti-rabbit or anti-mouse IgG (1:5000, Vector Laboratories). SuperSignal West Femto ECL (Pierce, #34096) was used to reveal the immunoreactive proteins, and images were acquired using a ChemiDoc MP (Bio-Rad). Luminescent immunoreactive protein bands were quantified using Fiji software (ImageJ)*(94)*. Density was normalized to GAPDH, and results are presented as the fold-change compared to wildtype average.

Immunohistochemistry

For cross-competition blocking experiments, PFA-fixed 40µm thick sections from a 5XFAD transgenic mouse (B6SJL-Tg(APPSwFlLon,PSEN1*M146L*L286V)6799Vas/Mmjax) were used. Free-floating sections were washed with 0.1 M phosphate buffer saline (PBS) in 0.1% triton (PBST) three times for 15 min and blocked with 2% bovine serum albumin (BSA) for 1h. For blocking experiments, prior to antibodies reactivity, sections were incubated with unlabeled CP-2 (25 µM) or PBS overnight. Sections were then washed with DDW three times for 10 min and incubated with NFA-Aβ-detecting A11 antibody (1:2500) in antibody buffer (PBST containing 2% BSA) overnight at 4°C. Sections were then washed with 1% PBST and incubated with Alexa Fluor 568 secondary goat anti-rabbit antibody (1:1000 Abcam) in antibody buffer for 1 h at room temperature. Sections were then stained with DAPI (4',6-diamidino-2-phenylindole dihydrochloride; 1:500, MP Biomedicals) and washed for 10 min in PBS with 0.1% TBST. Stained sections were mounted on super frost glass slides, embedded with ImmunoMount (Sigma-Aldrich, Switzerland), coverslipped, and stored in dark for microscopic images.

Free-floating sections were stained for immunofluorescence with anti-IBA1 immunohistochemistry (IHC) and were mounted onto slides for double-labeling. For anti-IBA1 IHC, sections were washed in PBS three times for 10 minutes and then blocked in PBST with 5% normal goat serum (NGS) for 1 hour at room temperature. Sections were incubated overnight at 4 °C in primary antibody anti-IBA1 (1:500, Wako, 019-19741) in PBST with 2% NGS. The tissues were subsequently washed in PBST, then incubated in PBS with 1% NGS and biotinylated secondary antibody. Sections were washed in PBS, then mounted and dried, before coverslipping and imaging with an Olympus BX61 microscope.

For double-labeling with anti-C1q and anti-PSD95, slides were rinsed three times for 10 minutes in PBS and then incubated in a citrate buffer for antigen retrieval. Sections for C1q complex (C1q) were incubated in the water bath at 85 ºC in citrate buffer with a pH of 9.5 for 30 minutes, followed by 20 minutes at room temperature. They were then rinsed again and placed in a dilution buffer containing 10% NGS and 0.4% Triton-X for 1 hour. One section from each animal was placed into primary antibody for anti-rat C3 (1:100, MP Biosciences, 55730) and another for anti-rabbit C1q (1:100, Abcam, ab182451). Both antibody solutions also contained anti-mouse

postsynaptic density protein (PSD95; 1:100, Millipore, MAB1596). Slides were incubated overnight at 4ºC. Following incubation, slides were rinsed and then incubated for one hour in secondary antibody solutions of anti-rabbit Alexafluor 488 (Invitrogen, A11034) and anti-mouse Alexafluor 594 (Invitrogen, A11032) or anti-rat Alexafluor 488 (Invitrogen, A11006) and anti-mouse Alexfluor 594. Slides were rinsed and coverslipped using Vectashield Vibrance with DAPI (Vector Laboratories, H-1800). Z-stack multi-channel images were taken at 63x using a Zeiss LSM 800 Confocal and Zen Blue software (v. 2.6, Carl Zeiss, Inc, Munich, Germany) and analyzed with Fiji Software (ImageJ).

Dynamic light scattering

To determine the size of NFA-Aβ before and after incubation with CP-7, a solution of Aβ (30 μM) in PBS was incubated in the absence or presence of cyclic peptide **7** (150 μM) for 72 h and the size of the particles was monitored by a Malvern Zetasizer Nano ZS instrument (Malvern, UK) operated with a 3 mW He−Ne laser source operating at a wavelength of 633 nm. Scattered light was detected at an angle of 173° (*99*).

Mitochondrial electron transport chain (mtETC) activities

The activities of mitochondrial complexes I (CI), II (CII), III (CIII), and IV (CIV) were assayed using a spectrophotometric enzyme activity assay (*104, 105*) performed on a FLUOstar Omega spectrophotometric plate reader (BMG). mtETC complex activities were measured and normalized to both citrate synthase (CS) activity and protein concentration. CS is a common readout for mitochondrial mass, and normalization of complex activities to CS activity can reveal actual alterations in activities of the complexes themselves, or alterations in their abundances within the mitochondria, while normalization of complex activities to total protein concentration of the homogenates can potentially reveal alterations in the mitochondrial mass within the tissue. About 10-20 mg of frozen brain tissue was homogenized in SEF Buffer (10 mM K_2HPO_4/KH_2PO_4, 250 mM sucrose, 2 mM EDTA), using a bead mill homogenizer and 1.5 mL microtubes pre-filled with 1.4 mm ceramic beads (Omni International).

Complex I (CI): Cell homogenates were incubated in a potassium phosphate (K_2HPO_4)-buffered solution of bovine serum albumin (BSA) in the presence of nicotinamide adenine dinucleotide (NADH), ubiquinone (CoQ), and the artificial electron receptor 2,6- dichlorophenolindophenol (DCPIP). Ubiquinone reduced to ubiquinol (QH2) by the oxidation of NADH to NAD+ by CI rapidly reduces DCPIP (blue) to DCIPIH2 (colorless). The NADH oxidation was assayed through spectrophotometric measurement of the extinction of DCPIP absorption at 600 nm over 17 minutes. Non-specific NADH oxidation was determined by simultaneously assaying NADH oxidation in each tissue homogenate in the presence of the potent CI inhibitor rotenone, and CI activity was calculated by subtracting the nonspecific (rotenone-inhibited) NADH oxidation from the total (rotenone-uninhibited) NADH oxidation.

Complex II (CII): Cell homogenates were incubated in a K_2HPO_4-buffered solution of BSA, ethylenediaminetetraacetic (EDTA), and sodium azide (NaAz) in the presence of succinate, decylubiquinone (DUB), adenosine triphosphate (ATP) and DCPIP. DUB reduced to DUH2 by the oxidation of succinate by CII rapidly oxidizes DCPIP (blue) to DCIPIH2 (colorless). Succinate oxidation was assayed through spectrophotometric measurement of the extinction of DCPIP absorbance at 600 nm for 15 minutes. Non-specific reduction of DCPIP was corrected for by simultaneously assaying each tissue homogenate in the presence of the potent CII inhibitor malonate, and CII activity was calculated by subtracting the nonspecific (malonate-inhibited) succinate oxidation from the total (malonate-uninhibited) succinate oxidation.

Complex III (CIII): Cell homogenates were incubated in a K_2HPO_4-buffered solution of EDTA, NaAz, and polysorbate 20 in the presence of reduced DUH2 and cytochrome C (CytC). Reduction of CytC by CIII via oxidation of DUH2 was assayed via spectrophotometric measurement of reduced CytC absorbance at 550 nm over 15 minutes. Non-specific reduction of CytC was corrected for by first assaying for CytC reduction in the presence of DUH2 but in the absence of the homogenate.

Complex IV (CIV): Cell homogenates were incubated in a K_2HPO_4-buffered solution in the presence of reduced CytC. The oxidation of reduced CytC by CIV was assayed via spectrophotometric measurement of the extinction of absorption by reduced CytC at 550 nm over 15 minutes. The reaction endpoint was assessed by artificially oxidizing all reduced CytC in the reaction mixture via the addition of the potent oxidizer potassium ferricyanide ($K_3Fe(CN)_6$), and the total reduced CytC in the reaction was quantified using a triplicate of blank wells lacking tissue homogenate.

Citrate Synthase (CS): Cell homogenates were incubated in a TrisHCl-buffered solution in the presence of oxaloacetic acid, acetyl-CoA, and 5,5′-dithiobis-(2-nitrobenzoic acid) (DTNB). CoA-SH generated by the condensation of acetyl-CoA and oxaloacetic acid by CS to citric acid rapidly cleaves DTNB (colorless) to TNB-, which rapidly ionizes to TNB2- (yellow). Condensation of acetyl-CoA and oxaloacetic acid by CS was assayed via spectrophotometric measurement of TNB2- at 411nm over 15 minutes. Protein concentration of cell homogenates was assayed using the Pierce BCA Protein Assay (Millipore).

Surface plasmon resonance (SPR) assays

All experiments were performed using a Biacore T200 (Cytiva) and carried out at 25ºC. The instrument was desorbed before use with the Biacore automated 'Desorb' routine. A CM5 sensor (Cytiva) was docked, running buffer changed to PBS-T and the sensor cleaned with a 30 second injection of 50 mM NaOH (0.22 µm filtered; 10 µl/min flow rate). Aβ42 fibrils were prepared at 20 µg/ml and Aβ42 NFAs at 4 or 20 µg/ml in 10 mM sodium acetate buffer at pH 5.5, 5.0, 4.5 or 4.0. The proteins were injected onto the sensor surface at 10 µl/min for 120 seconds to confirm the optimum immobilization pH. The sensor surface was then cleaned with a 30 second

injection of 50 mM NaOH. Aβ42 oligomers could not be pre-concentrated onto the sensor surface and could not be immobilized by amine coupling.

Aβ42 NFAs, Aβ42 fibrils, A11 antibody and BSA were immobilized on the sensor surface by direct amine coupling. Reference or active channel surfaces were activated for 7 minutes with a 1:1 mixture comprising 200 mM 1-Ethyl-3-(3-dimethylaminopropyl)carbodiimide (EDC) and 50 mM N-Hydroxysuccinimide (NHS). Aβ42 fibrils (Fc2), A11 antibody (Fc3) and Aβ42 NFAs were coupled to the active channel surfaces. BSA was coupled to the reference channel surface on Fc1. All unreacted EDC-NHS groups were then inactivated with a 7-minute injection of 1 M ethanolamine. All solutions were injected onto the relevant flow channel at a rate of 10 µl/min.

CP-2 was prepared as a stock solution in DMSO. For CP-2 binding assays, running buffer was changed to PBS-T with 1% DMSO. For all other binding assays running buffer was PBS-T. Analytes were injected onto reference (Fc1) and protein immobilized channels (Fc2, Fc3, Fc4) for 120 seconds and dissociated in running buffer for 180 seconds. The sensor surface was regenerated with a 30 second injection of 10 mM glycine pH 1.5. Samples were injected in ascending concentration series and in duplicate at each concentration. Vehicle control injections were included before and after the analyte binding series for buffer blank subtraction.

Binding response data were analyzed using Biacore T200 Evaluation software. Binding responses were reference channel subtracted (i.e., Fc2-Fc1, Fc3-Fc1, Fc4-Fc1 as appropriate) and buffer blank subtracted (double referenced). Response amplitude was then averaged over a 5 second window, 5 seconds before the end of analyte sample injection of the double reference subtracted binding responses.

Online Supplemental Results

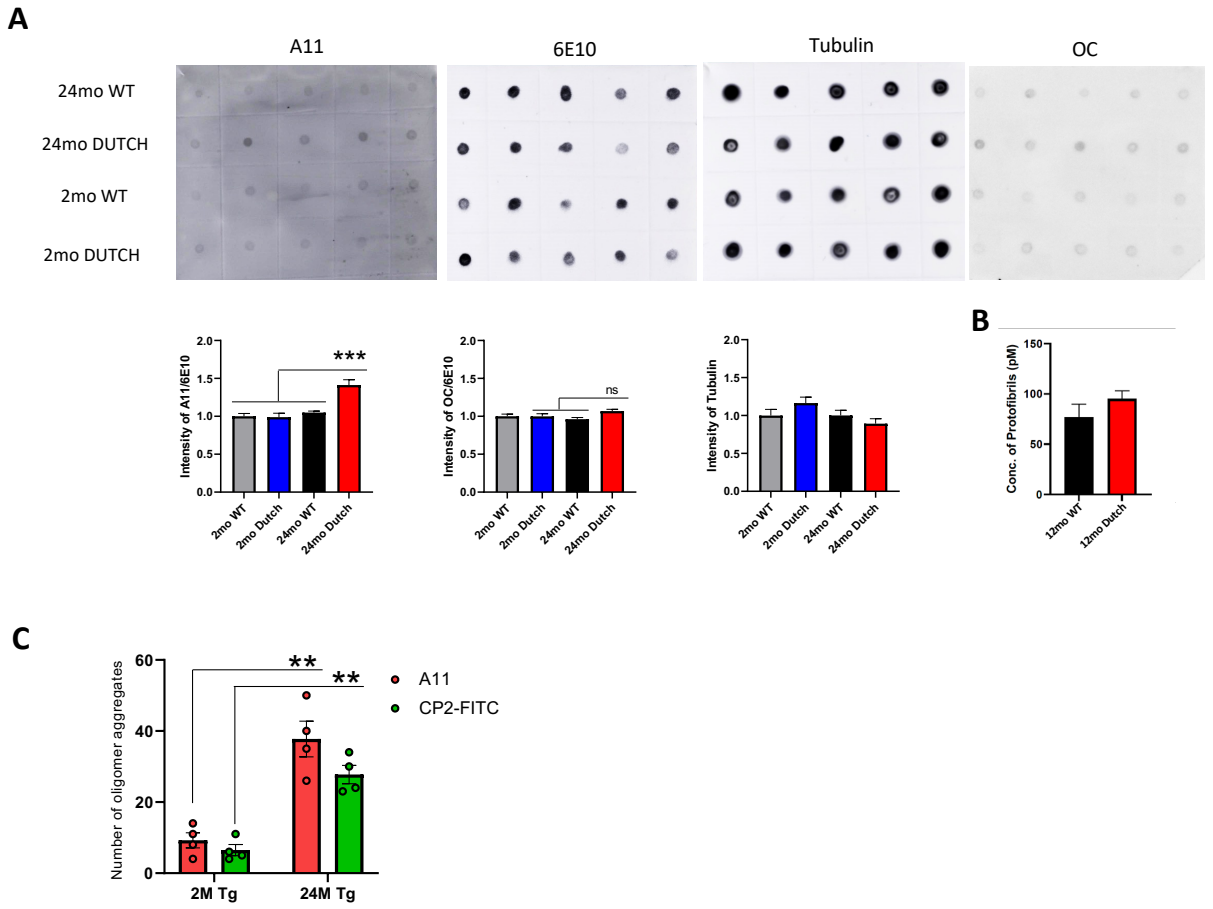

Figure S1. Quantification of dot blot assay and quantification of A11 and OC epitomic IHC and CP-2-FITC fluorescence microscopy from Figure 1. (A) Dot blot assay with quantification for A11/6E10 ratio, OC/6E10 ratio and α-tubulin levels across all groups. (B) Quantification of mAb158 sandwich assay showing no differences in Aβ PF concentration between TBS soluble brain fractions extracted from 12-month-old Dutch (n=3/sex) and wildtype (n=1/sex) mice. (C) Quantification of A11 IHC, and CP-2-FITC(*22*) comparing 2- and 24-month old Dutch mice.

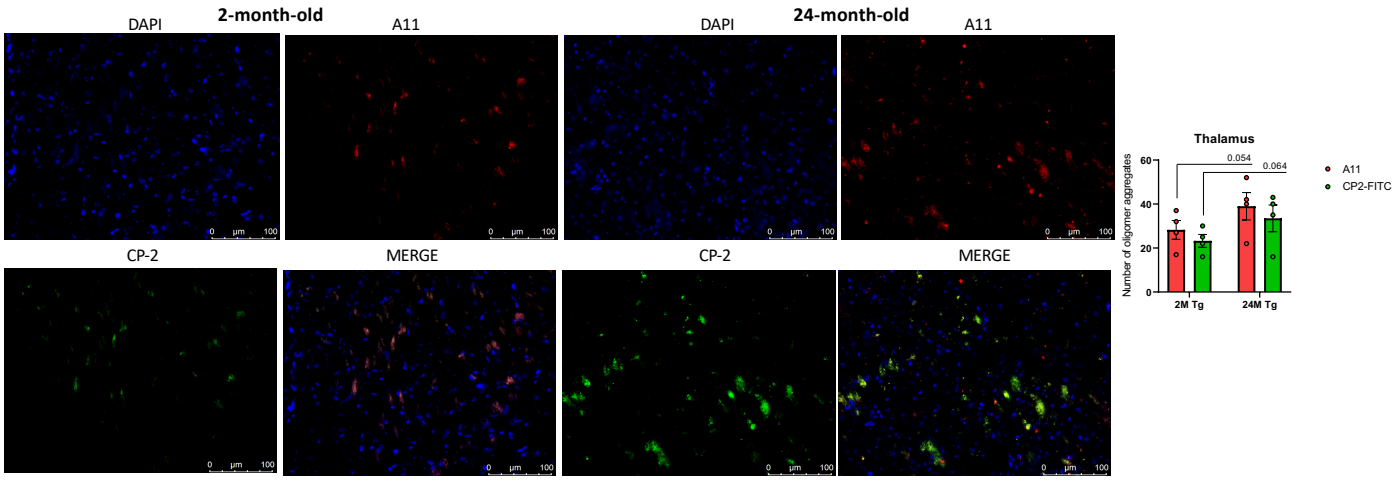

Figure S2. Dutch mice show aging-related accumulation of NFA-Aβ in the thalamus using DAPI, A11 immunohistochemistry, and CP-2-FITC fluorescence microscopy(*22*)**.**

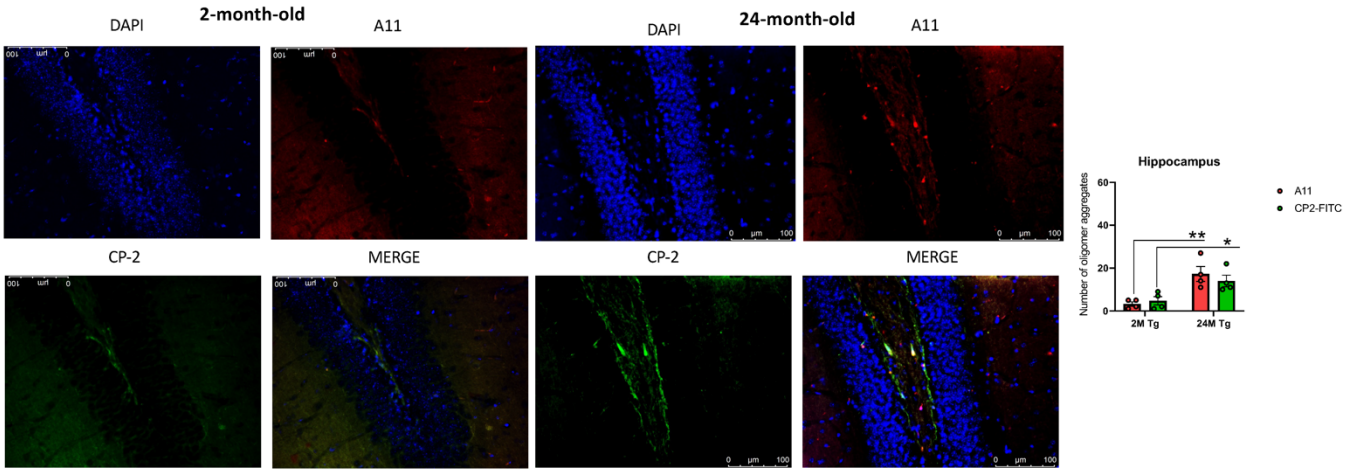

Figure S3. Dutch mice show aging-related elevation of levels of NFA-Aβ in the hippocampus using DAPI, A11 immunohistochemistry, and CP-2-FITC fluorescence microscopy(*22*)**.**

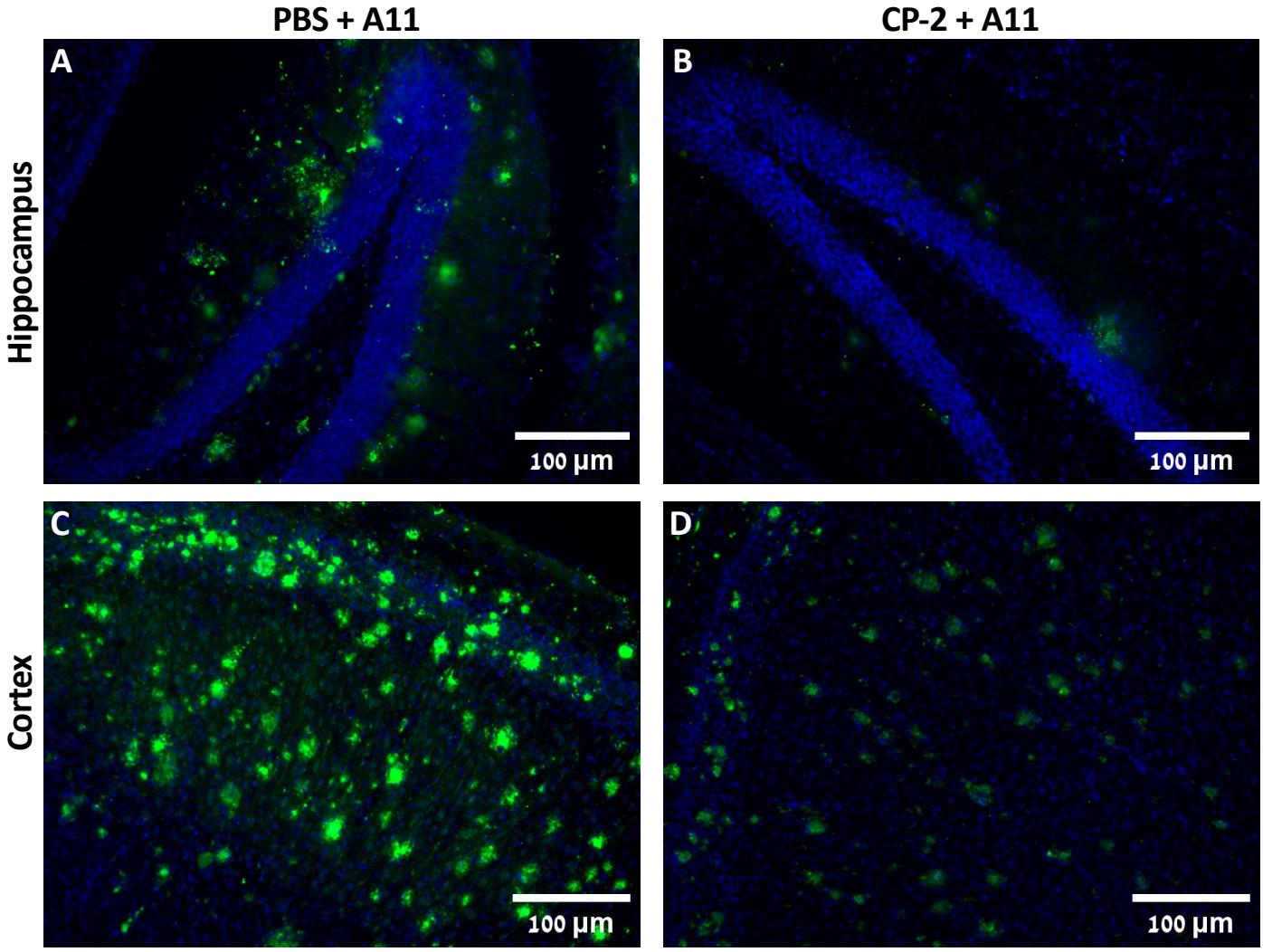

Figure S4. CP-2 cyclic peptide binding alters binding of NFA-Aβ-detecting A11 antibody. Representative immunofluorescence image of adjacent sections of the (A-B) hippocampus and (C-D) cortex of the same 7-month-old 5xFAD mouse brain stained with NFA-Aβ-detecting A11 antibody in presence of either PBS (A and C) or excess cyclic peptide CP-2 (B and D).

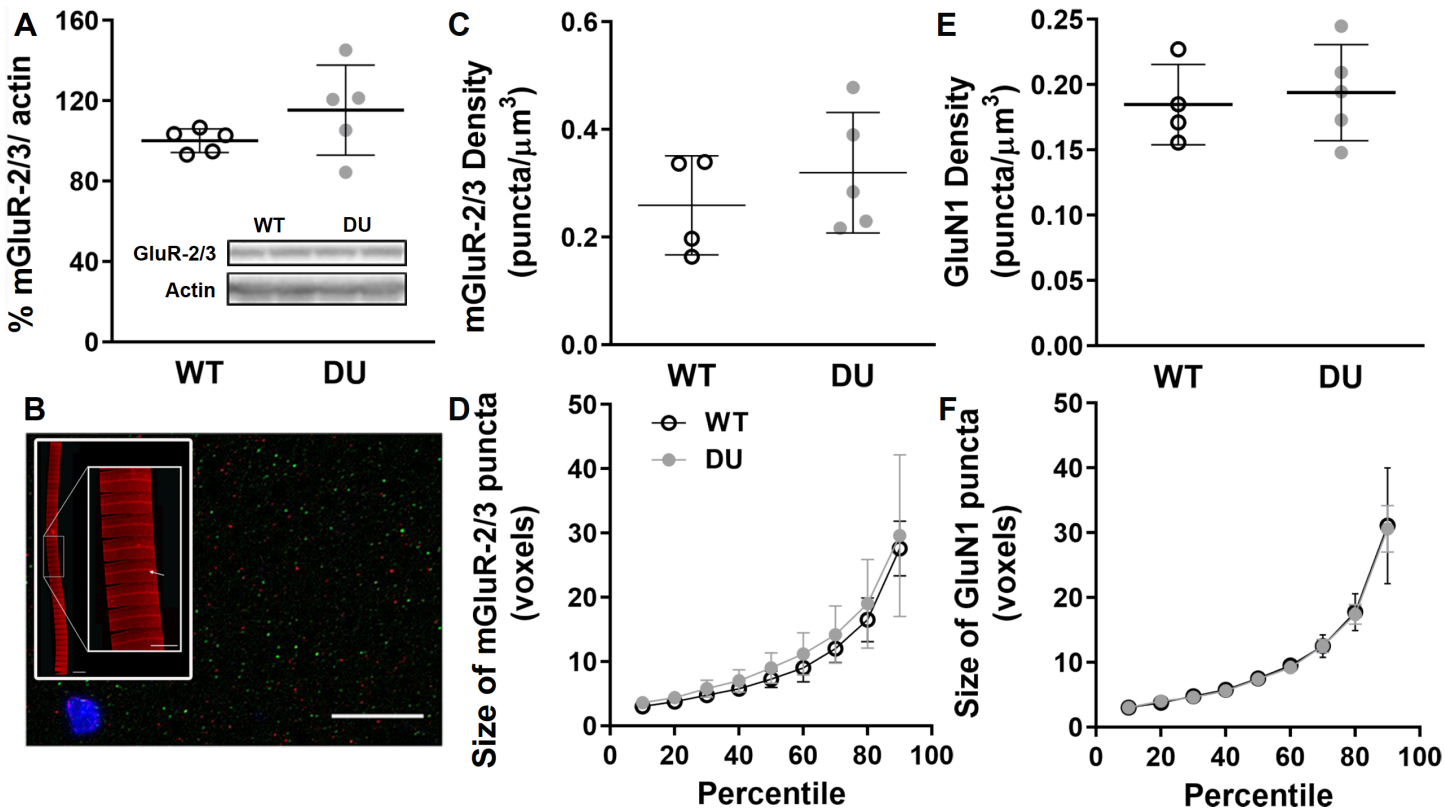

Figure S5. No change in expression of mGluR-2/3 in the hippocampus of wildtype and Dutch mice. (A) Densitometric quantification of mGluR-2/3 normalized to actin from 12-month-old wildtype and Dutch mice and expressed as a percentage of the protein level in wildtype mice with example western blot. Data are mean ± SD from n = 5 wildtype and n = 5 Dutch mice. **(B)** Higher magnification of a single 70 nm section, showing synaptic puncta of mGluR-2/3 (green) and GluN1 (red), along with a nucleus stained with DAPI. Cell bodies stained with Neurotrace were used as landmarks for alignment. Scale bar = 10 µm. Large Inset is an example of serial sections stained with Neurotrace and imaged at 10x for array tomography. The images were stitched together to render a full-length depiction of a typical sample. Small Inset is magnifying the area of serial sectioning in the box; arrow indicates the CA1 cell layer. Scale bars = 1 mm and 0.5 mm (inset). **(C)** Density of synaptic puncta immunoreactive for mGluR-2/3 were similar in 12-month-old wildtype and Dutch mice. Data are mean ± SD. **(D)** Distribution of puncta sizes was comparable between the two genotypes for mGluR-2/3 synapses. Data are mean ± SEM from n = 4 wildtype and n = 5 Dutch mice. **(E)** Density of synaptic puncta immunoreactive for GluN1 were similar in 12-month-old wildtype and Dutch mice. Data are mean ± SD. **(F)** Distribution of puncta sizes was comparable between the two genotypes for GluN1 synapses. Data are mean ± SEM. The puncta were assessed from n = 4 wildtype n = 5 Dutch mice.

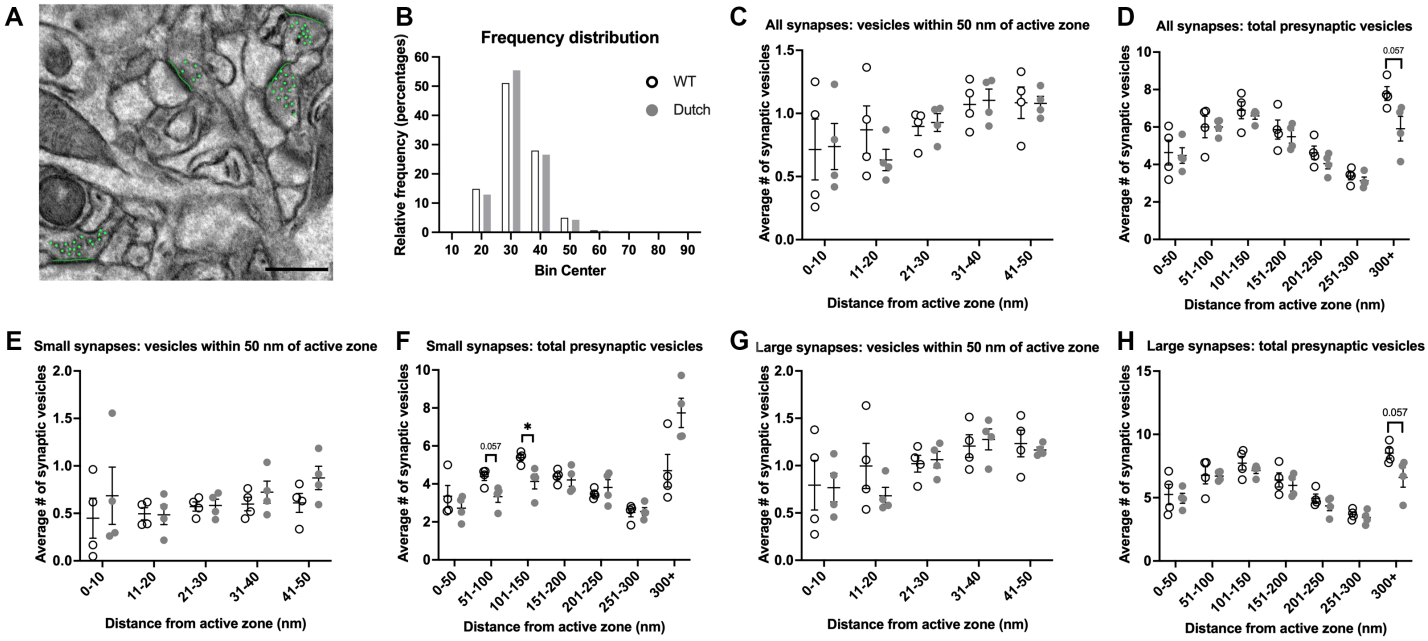

Figure S6. Synaptic vesicle size, number, and distribution are comparable in the CA1 of 12-month-old wildtype and Dutch mice. (A) Representative EM micrograph of presynaptic vesicles. Green dots indicate vesicles in the presynaptic terminal and the green line indicates the PSD, as described in the Methods section. Scale bars = 400 nm. **(B)** Frequency distribution of vesicle size. (**C-D**) Average counts of synaptic vesicles within 50 nm from the active zone or total vesicles at the presynaptic terminal of all synapses. (**E-F**) Average counts of synaptic vesicles within 50 nm from the active zone or total vesicles at the presynaptic terminal of synapses with a head diameter <0.4mm (small, thin synapses). (**G-H**) Average counts of synaptic vesicles within 50 nm from the active zone or total vesicles at the presynaptic terminal of synapses with a head diameter >0.4mm (large, mushroom synapses). Data are mean ± SD from wildtype (n = 4) and Dutch (n = 4) (Multiple Mann-Whitney).

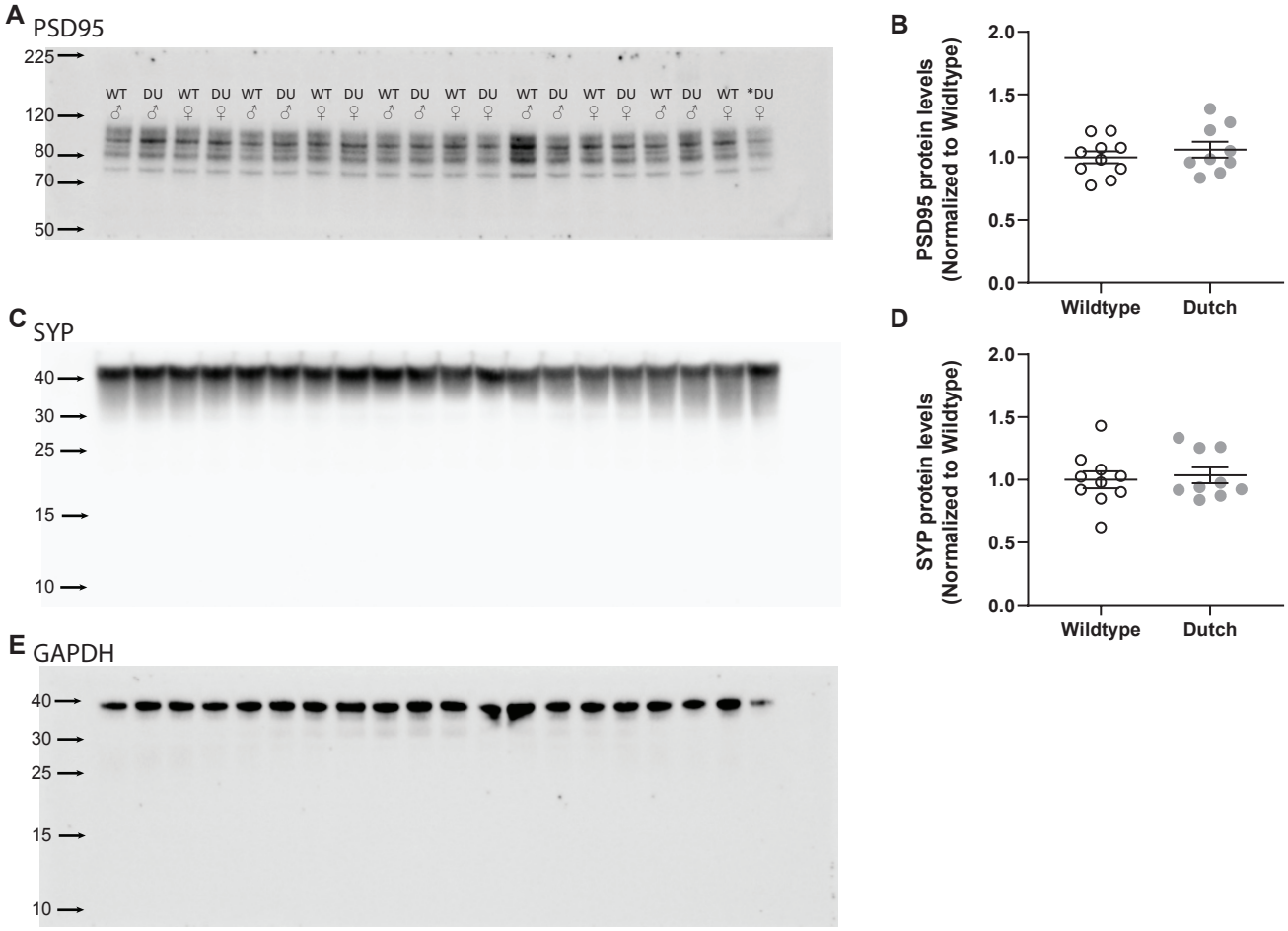

Figure S7. No differences in levels of synaptic markers between Dutch and wildtype mice. (A) Western blot images for postsynaptic density protein 95 (PSD95) of hippocampal lysates from 12-month-old wildtype and Dutch mice of both sexes. **(B)** Densitometric quantification of PSD95 normalized to GAPDH and normalized to the protein level in wildtype mice. **(C)** Western blot images for synaptophysin (SYP) of hippocampal lysates from 12-month-old wildtype and Dutch mice of both sexes. **(D)** Densitometric quantification of SYP normalized to GAPDH and normalized to the protein level in wildtype mice. **(E)** Western blot images for GAPDH of hippocampal lysates from 12-month-old wildtype and Dutch mice of both sexes. Data are mean ± SEM from n = 10 wildtype (5M and 5F) and n = 9 Dutch mice (5M and 4F). *DU was excluded from all quantification as an outlier.

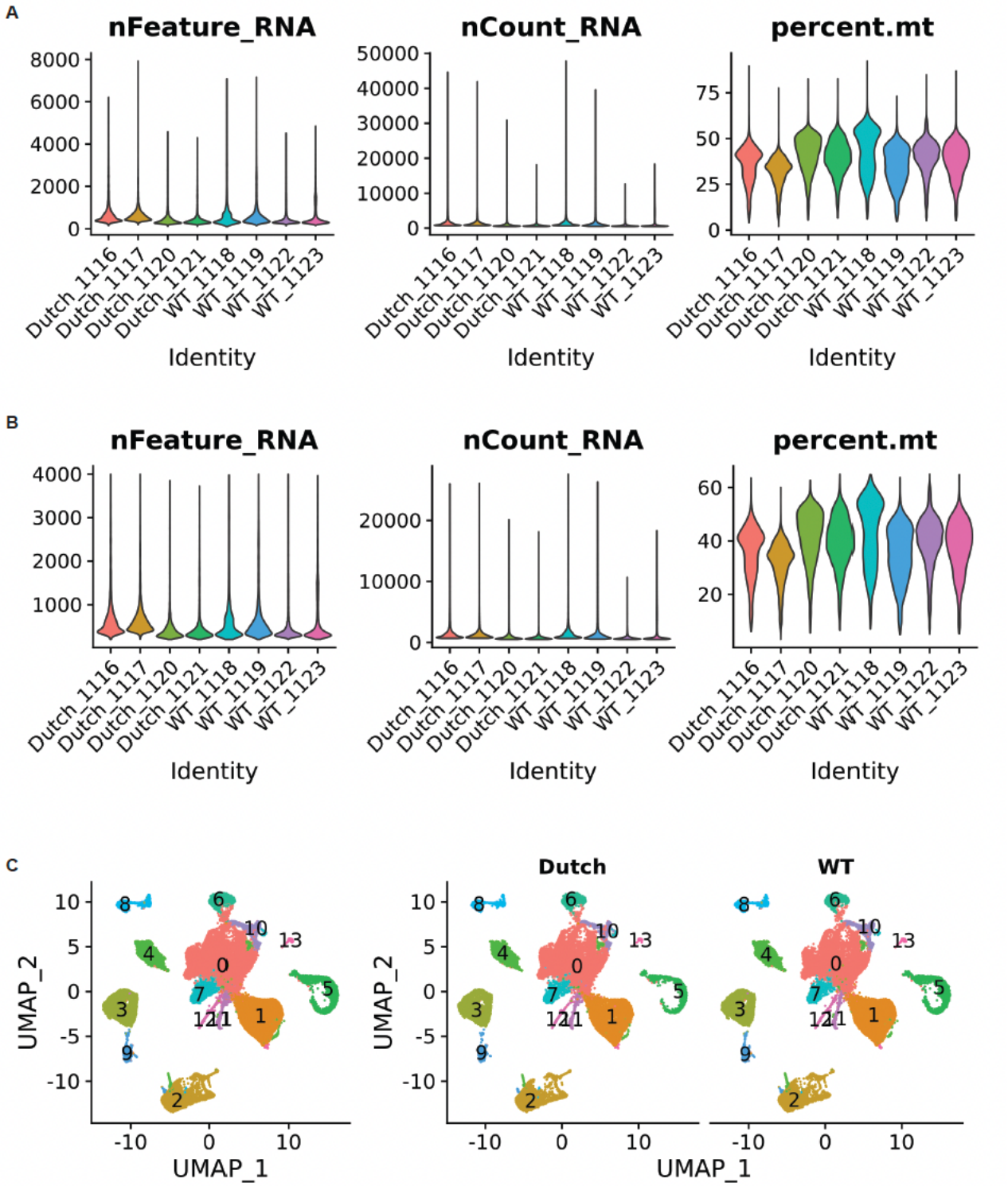

Figure S8. Quality control filtering of scRNA-Seq data. (A) Raw data values and **(B)** filtered values for nFeatures (left), nCounts (center) and % mitochondria reads (right) for the samples. **(C)** UMAP from Figure 6 with split UMAPs for Dutch and wildtype samples.

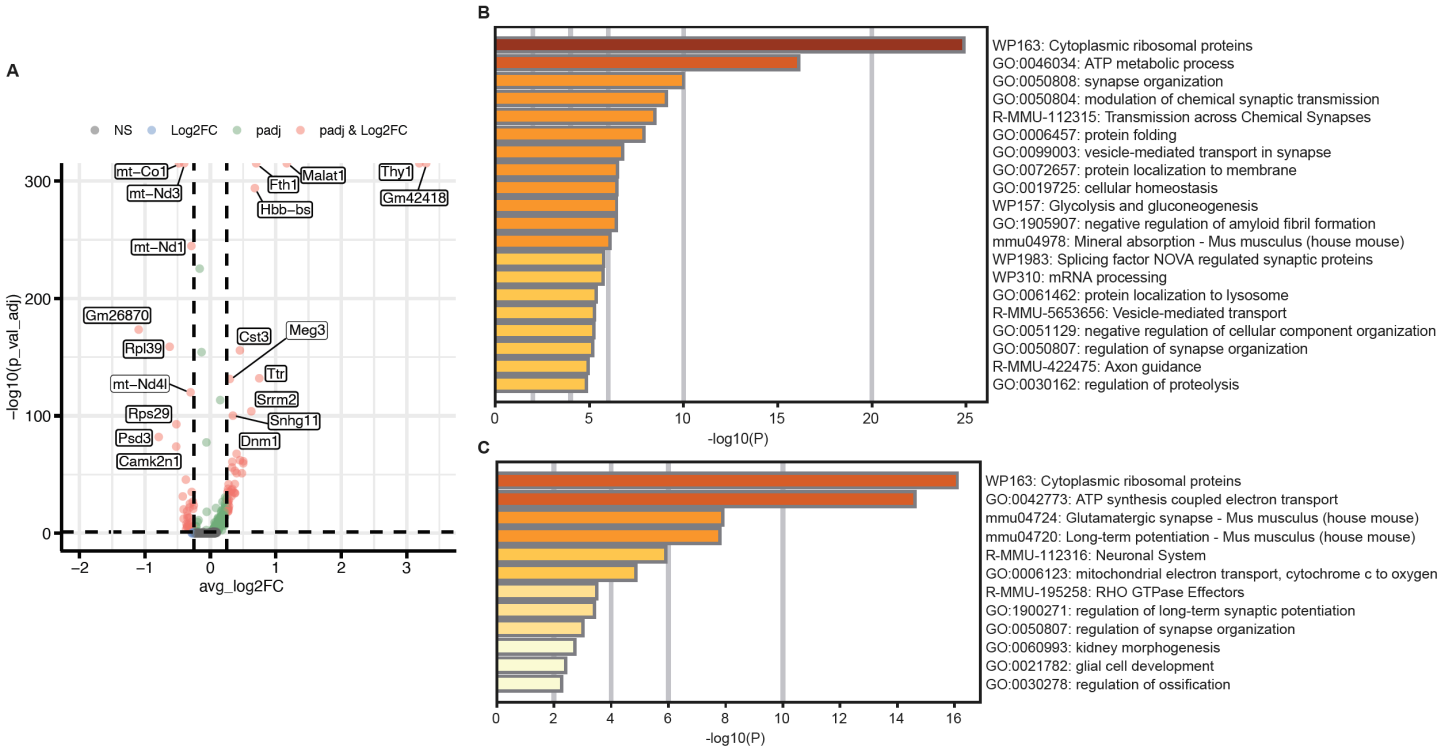

Figure S9. Transcriptional profile of Cluster 0- excitatory neurons is altered in Dutch mice. (A) Volcano plot of genes enriched in Cluster 0 as calculated by pseudobulk differential expression analysis. Red genes are Log2FC > 0.25 and adj. p-value < 0.05, blue Log2FC < 0.25 and adj. p-value < 0.05, green genes are Log2FC > 0.25 and adj. p-value > 0.05, and grey genes are Log2FC < 0.25 and adj. p-value > 0.05. **(B-C)** GO term analysis of **(B)** up-regulated and **(C)** down-regulated genes enriched in Cluster 0 (adj. p-value < 0.05) using metascape(*91*).

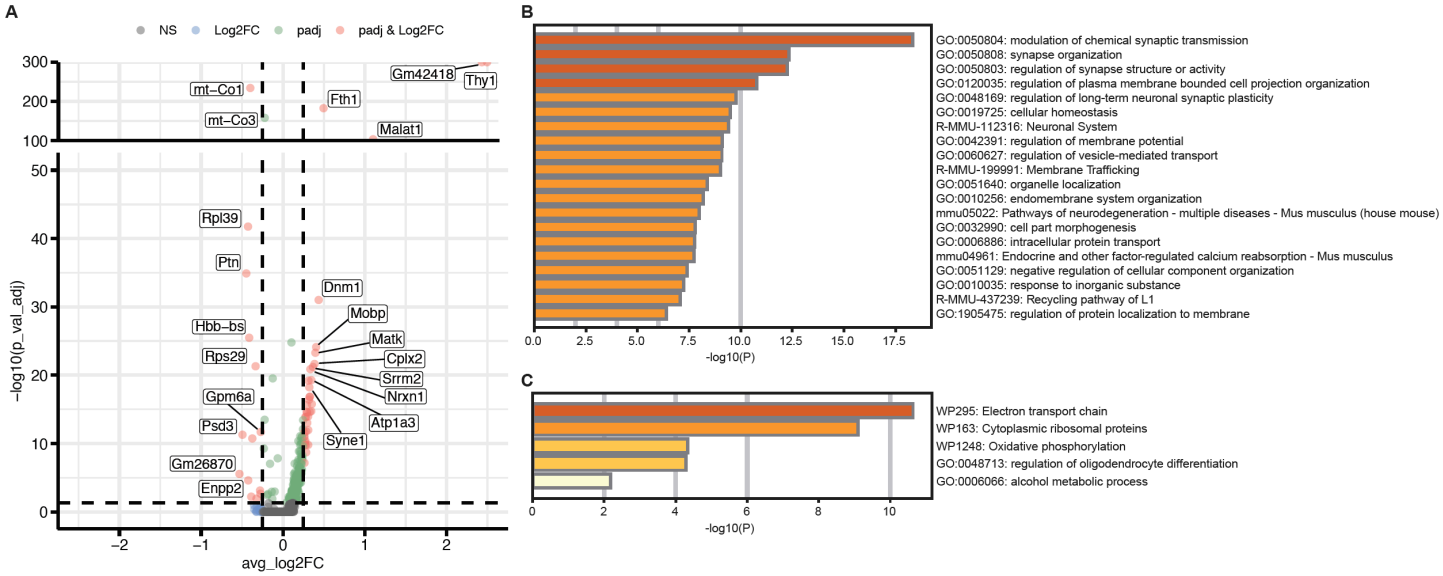

Figure S10. Transcriptional profile of Cluster 1- astrocytes is altered in Dutch mice. (A) Volcano plot of genes enriched in Cluster 1 as calculated by pseudobulk differential expression analysis. Red genes are Log2FC > 0.25 and adj. p-value < 0.05, blue Log2FC < 0.25 and adj. p-value < 0.05, green genes are Log2FC > 0.25 and adj. p-value > 0.05, and grey genes are Log2FC < 0.25 and adj. p-value > 0.05. **(B-C)** GO term analysis of **(B)** upregulated and **(C)** downregulated genes enriched in Cluster 1 (adj. p-value < 0.05) using metascape(*91*).

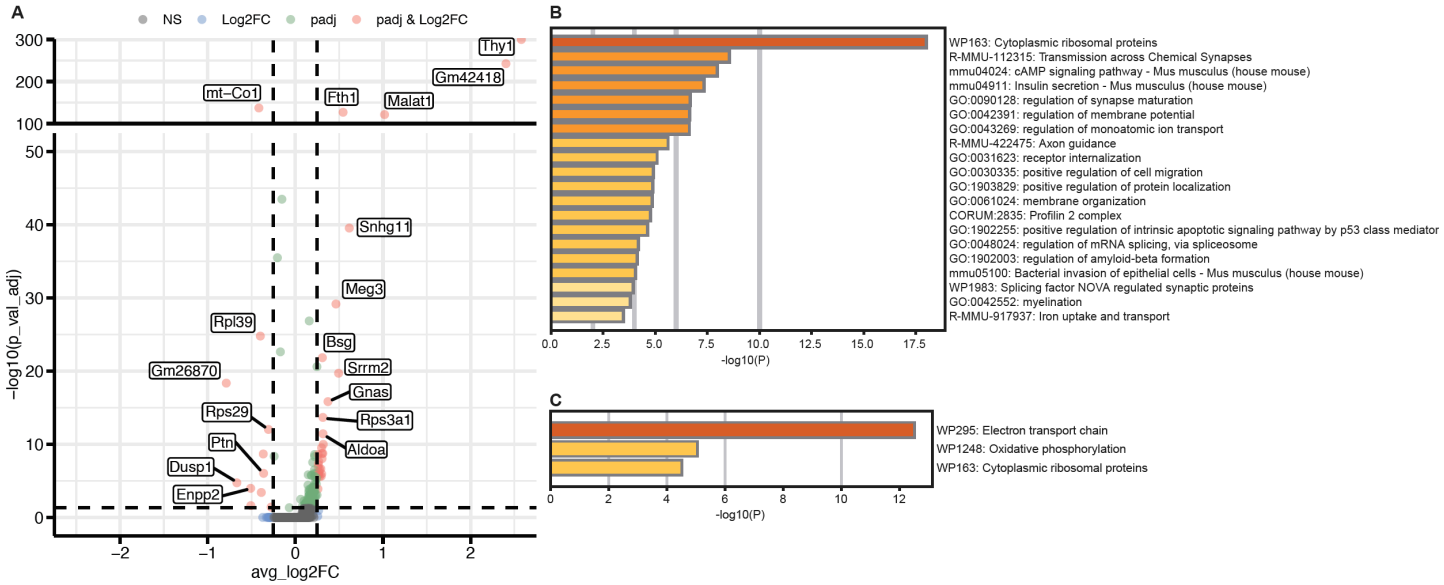

Figure S11. Transcriptional profile of Cluster 3 endothelial cells is altered in Dutch mice. (A) Volcano plot of genes enriched in Cluster 3 as calculated by pseudobulk differential expression analysis. Red genes are Log2FC > 0.25 and adj. p-value < 0.05, blue Log2FC < 0.25 and adj. p-value < 0.05, green genes are Log2FC > 0.25 and adj. p-value > 0.05, and grey genes are Log2FC < 0.25 and adj. p-value > 0.05. **(B-C)** GO term analysis of **(B)** upregulated and **(C)** downregulated genes enriched in Cluster 3 (adj. p-value < 0.05) using metascape(*91*).

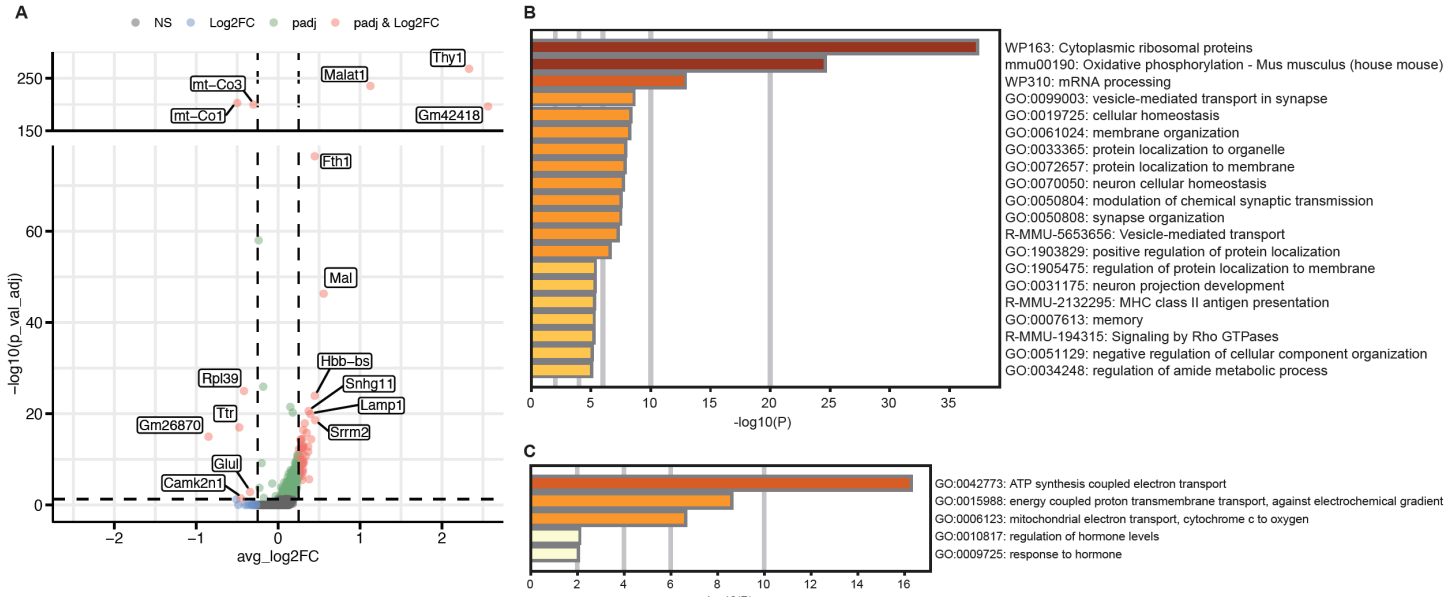

Figure S12. Transcriptional profile of Cluster 4 oligodendrocytes is altered in Dutch mice. (A) Volcano plot of genes enriched in Cluster 4 as calculated by pseudobulk differential expression analysis. Red genes are Log2FC > 0.25 and adj. p-value < 0.05, blue Log2FC < 0.25 and adj. p-value < 0.05, green genes are Log2FC > 0.25 and adj. p-value > 0.05, and grey genes are Log2FC < 0.25 and adj. p-value > 0.05. **(B-C)** GO term analysis of **(B)** upregulated and **(C)** downregulated genes enriched in Cluster 4 (adj. p-value < 0.05) using metascape(*91*).

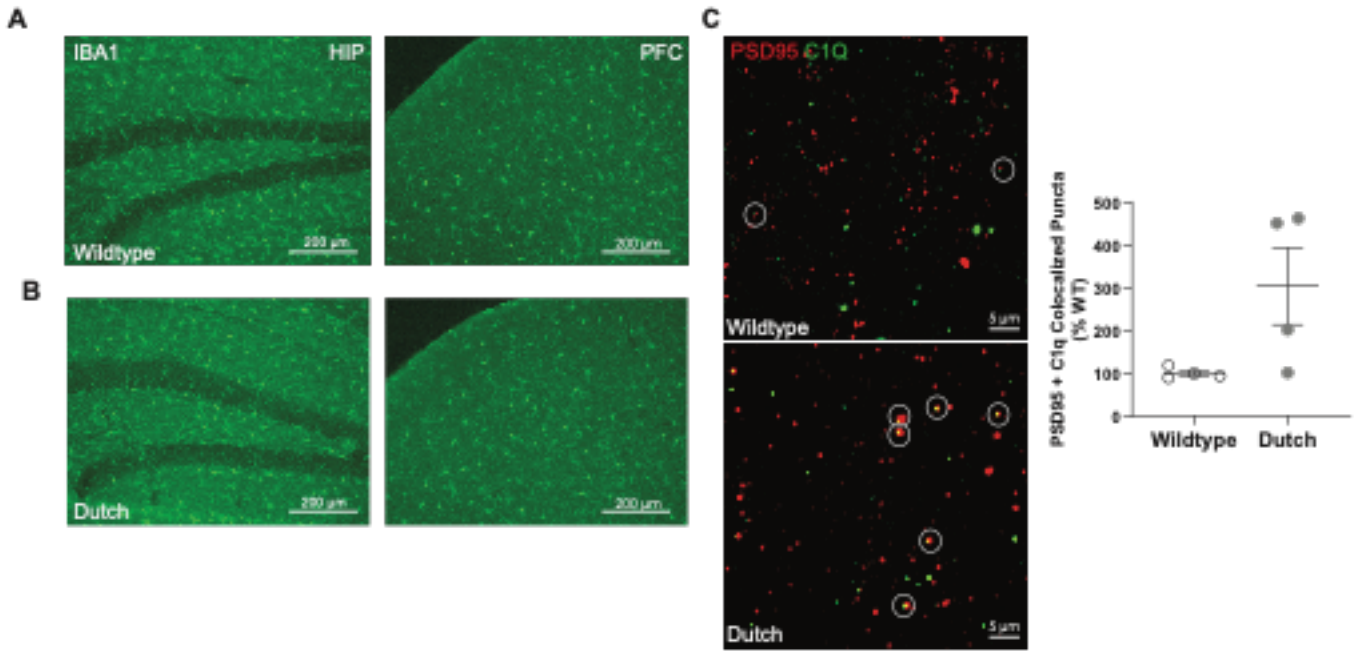

Figure S13. No differences in microgliosis or C1q co-localization with synaptic puncta in Dutch mice. (A-B) Representative images of anti-IBA1 IHC in hippocampus (HIP, left) and prefrontal cortex (PFC, right) from 12-month-old wildtype (A) and Dutch mice (B) showed no difference in microgliosis. **(C)** Confocal images of PSD95 (red) and C1q (green) in 12-month-old wildtype and Dutch mice CA1 with quantification of colocalized PSD95- and C1q-immunoreactive puncta (right) revealing differences were not significant. Data are mean ± SEM from n = 4 males for each genotype.

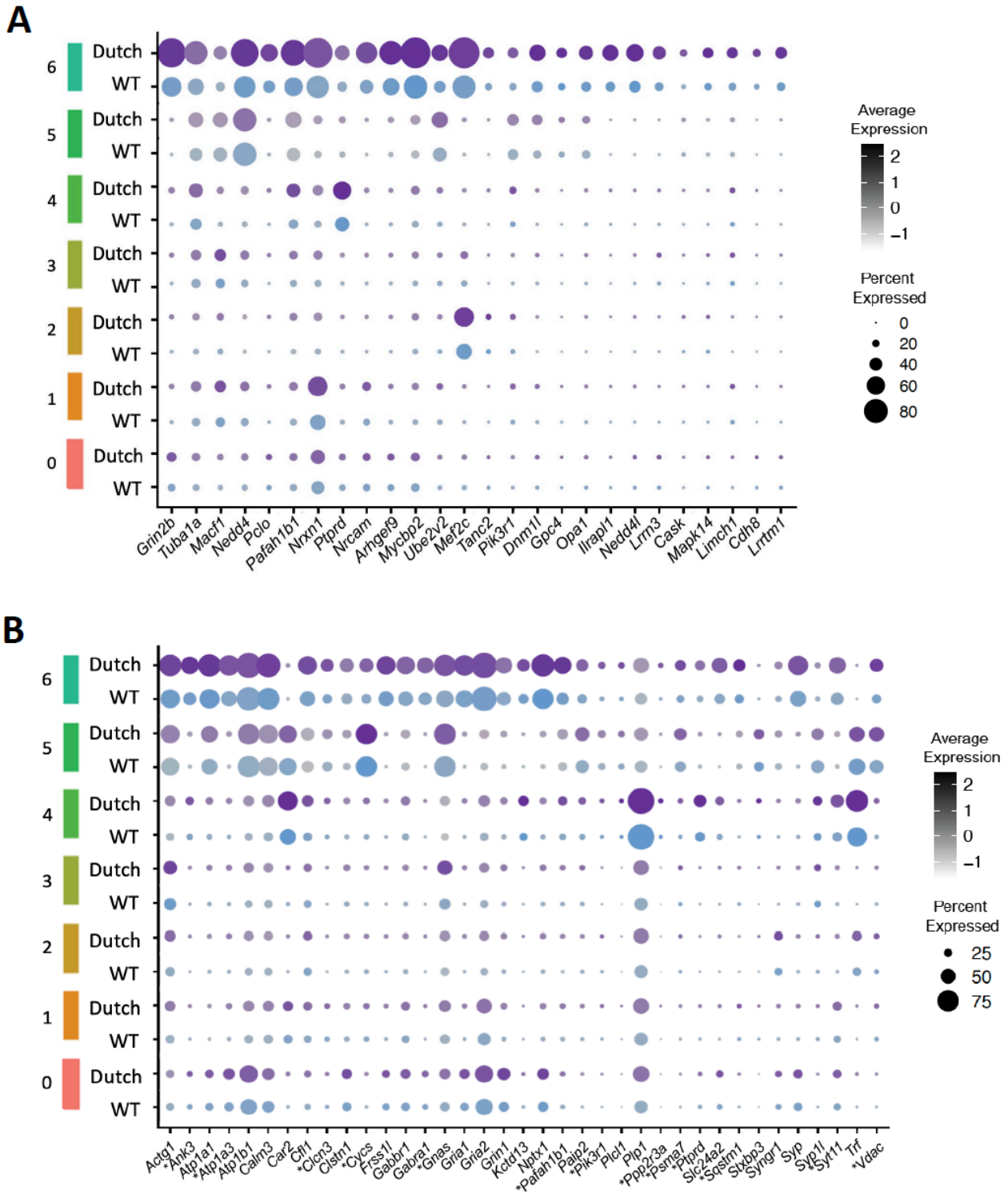

Figure S14. Biological Processes associated with synaptic transmission are altered in excitatory neurons and oligodendrocytes. (A-B) Dot plot of genes associated with upregulated GO terms **(A)** "regulation of synapse organization" from Cluster 6 excitatory neurons and **(B)** "modulation of chemical synaptic transmission", from Cluster 4 oligodendrocytes, split into Dutch and wildtype mice across all clusters. Wildtype mice are in blue, Dutch mice are in purple. In B, genes marked with an asterisk have adj. $p<0.05$ in Cluster 6.

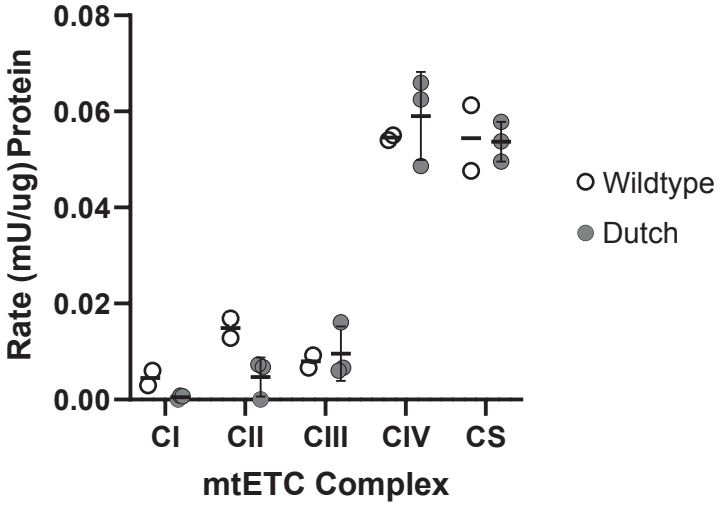

Figure S15. Mitochondrial complex I (CI), complex II (CII), complex III (CIII), complex IV (CIV), and citrate synthase activities in the hippocampi of wildtype (open circle) and Dutch (solid circle) mice at age 12 months. See also Supplemental Tables 8 and 9. For comparison of CI in wildtype vs Dutch, p=0.0355 when standardized to μg protein or p=0.0197 when standardized to mU/ml of citrate synthase (CS) and analyzed using an unpaired t test.